

Quantitative Spectroscopy of 24 A supergiants in the Sculptor galaxy NGC 300¹: Flux weighted gravity luminosity relationship, metallicity and metallicity gradient

Rolf-Peter Kudritzki

Institute for Astronomy, 2680 Woodlawn Drive, Honolulu, HI 96822; kud@ifa.hawaii.edu

Miguel A. Urbaneja

Institute for Astronomy, 2680 Woodlawn Drive, Honolulu, HI 96822; urbaneja@ifa.hawaii.edu

Fabio Bresolin

Institute for Astronomy, 2680 Woodlawn Drive, Honolulu, HI 96822; bresolin@ifa.hawaii.edu

Norbert Przybilla

*Dr. Remeis-Sternwarte Bamberg, Sternwartstr. 7, D-96049 Bamberg, Germany;
przybilla@sternwarte.uni-erlangen.de*

Wolfgang Gieren

*Universidad de Concepción, Departamento de Física, Casilla 160-C, Concepción, Chile;
wgieren@astro-udec.udec.cl*

and

Grzegorz Pietrzyński

*Universidad de Concepción, Departamento de Física, Casilla 160-C, Concepción, Chile;
pietrzyn@hubble.cfm.udec.cl*

ABSTRACT

A quantitative spectral analysis of 24 A supergiants in the Sculptor Group spiral galaxy NGC 300 at a distance of 1.9 Mpc is presented. A new method is introduced to analyze low resolution ($\sim 5\text{\AA}$) spectra, which yields metallicities accurate to 0.2 dex including the uncertainties arising from the errors in T_{eff} (5%) and $\log g$ (0.2 dex). For the first time the stellar metallicity gradient based on elements such as titanium

¹Based on VLT observations for ESO Large Programme 171.D-0004.

and iron in a galaxy beyond the Local Group is investigated. Solar metallicity is measured in the center and 0.3 solar in the outskirts and a logarithmic gradient of -0.08 dex/kpc. An average reddening of $E(B-V) \sim 0.12$ mag is obtained, however with a large variation from 0.07 to 0.24 mag. We also determine stellar radii, luminosities and masses and discuss the evolutionary status. Finally, the observed relationship between absolute bolometric magnitudes M_{bol} and flux weighted gravities $g_F = g/T_{eff}^4$ is investigated. At high temperatures the strengths of the Balmer lines depends solely on the flux-weighted gravity, which allows a precise direct determination of $\log g_F$ with an accuracy of 0.05 to 0.1 dex. We find a tight relationship between M_{bol} and $\log g_F$ in agreement with stellar evolution theory. Combining these new results with previous work on Local Group galaxies we obtain a new flux weighted gravity luminosity relationship (FGLR), which is very well defined and appears to be an excellent alternative tool to determine distances to galaxies.

Subject headings: galaxies: — distances galaxies: abundances — galaxies: stellar content — galaxies: individual (NGC300) — stars: early-type

1. Introduction

It has long been the dream of stellar astronomers to study individual stellar objects in distant galaxies to obtain detailed spectroscopic information about the star formation history and chemodynamical evolution of galaxies and to determine accurate distances based on the determination of stellar parameters and interstellar reddening and extinction. The most promising objects for such studies are massive stars in a mass range between 15 to $40 M_{\odot}$ in the short-lived evolutionary phase, when they leave the hydrogen main-sequence and cross the HRD in a few thousand years as blue supergiants of late B and early A spectral type. Because of the strongly reduced absolute value of bolometric correction when evolving towards smaller temperature these objects increase their brightness in visual light and become the optically brightest stars in the universe with absolute visual magnitudes up to $M_V \cong -9.5$ rivaling with the integrated light brightness of globular clusters and dwarf spheroidal galaxies.

There has been a long history of quantitative spectroscopic studies of these extreme objects. In a pioneering and comprehensive paper on Deneb Groth (1961) was the first to obtain stellar parameters and detailed chemical composition. This work was continued by Wolf (1971), Wolf (1972), Wolf (1973) in studies of A supergiants in the Milky Way and the Magellanic Clouds. Kudritzki (1973) using newly developed NLTE model atmospheres found that at the low gravities and the correspondingly low electron densities of these objects effects of departures from LTE can become extremely important. With strongly improved model atmospheres Venn (1995a),

Venn (1995b) and Aufdenberg et al. (2002) continued these studies in the Milky Way. Most recently, Przybilla et al. (2006) used very detailed NLTE line formation calculations including ten thousands of lines in NLTE (see also Przybilla et al. 2000, Przybilla et al. 2001a, Przybilla et al. 2001b, Przybilla & Butler 2001, Przybilla 2002) to determine stellar parameters and abundances with hitherto unknown precision (T_{eff} to $\leq 2\%$, $\log g$ to ~ 0.05 dex, individual metal abundances to ~ 0.05 dex). At the same time, utilizing the power of the new 8m to 10m class telescopes, high resolution studies of A supergiants in many Local Group galaxies were carried out by Venn (1999) (SMC), McCarthy et al. (1995) (M33), McCarthy et al. (1997) (M31), Venn et al. (2000) (M31), Venn et al. (2001) (NGC 6822), Venn et al. (2003) (WLM), and Kaufer et al. (2004) (Sextans A) yielding invaluable information about the stellar chemical composition in these galaxies.

The concept to go beyond the Local Group and to study A supergiants by means of quantitative spectroscopy in galaxies out to the Virgo cluster has been first presented by Kudritzki, Lennon & Puls (1995) and Kudritzki (1998). Following-up on this idea, Bresolin et al. (2001) and Bresolin et al. (2002) used the VLT and FORS at 5 \AA resolution for a first investigation of blue supergiants in NGC 3621 (6.7 Mpc) and NGC 300 (1.9 Mpc). They were able to demonstrate that for these distances and at this resolution spectra of sufficient S/N can be obtained allowing for the quantitative determination of stellar parameters and metallicities. Kudritzki, Bresolin & Przybilla (2003) extended this work and showed that stellar gravities and temperatures determined from the spectral analysis can be used to determine distances to galaxies by using the correlation between absolute bolometric magnitude and flux weighted gravity $g_F = g/T_{eff}^4$ (FGLR). However, while these were encouraging steps towards the use of A supergiants as quantitative diagnostic tools of galaxies beyond the Local Group, the work presented in these papers had still a fundamental deficiency. At the low resolution of 5 \AA it is not possible to use ionization equilibria for the determination of T_{eff} in the same way as in the high resolution work mentioned in the previous paragraph. Instead, spectral types were determined and a simple spectral type - temperature relationship as obtained for the Milky Way was used to determine effective temperatures and then gravities and metallicities. Since the spectral type - T_{eff} relationship must depend on metallicity (and also gravities), the method becomes inconsistent as soon as the metallicity is significantly different from solar (or the gravities are larger than for luminosity class Ia) and may lead to inaccurate stellar parameters. As shown by Evans & Howarth (2003), the uncertainties introduced in this way could be significant and would make it impossible to use the FGLR for distance determinations. In addition, the metallicities derived might be unreliable. This posed a serious problem for the the low resolution study of A supergiants in distant galaxies.

In this paper we present a solution to this problem and provide the first self-consistent determination of stellar parameters and metallicities for A supergiants in galaxies beyond the Local Group based on the quantitative model atmosphere analysis of low resolution spectra. We apply our new method on 24 supergiants of spectral type B8 to A5 in the Scultor Group spiral galaxy

NGC 300 and obtain temperatures, gravities, metallicities, radii, luminosities and masses. Note that while we have included a number of late type B supergiants in this work, we refer to the whole sample as “A supergiants” in the following, for reasons of simplicity. We will compare some of our results with the work by Urbaneja et al. (2005), who performed a quantitative study of six early B-type supergiants (B0.5 to B3). We will refer to those objects as “B supergiants”. The reason for this simplifying distinction is the difference in the analysis method. The temperatures of the B supergiants (in this nomenclature) are determined from the ionization equilibria of helium and silicon and metallicities result from the fit of individual spectral lines of α -elements such as oxygen, magnesium, silicon and carbon, whereas the temperatures of the A supergiants are obtained from the Balmer jump and the metallicities are determined from the spectral synthesis of many overlapping lines of different species including heavy elements such as iron, chromium and titanium.

The paper is organized as follows. After a brief description of the observations in section 2 we provide a detailed discussion of the analysis method, i.e. the determination of T_{eff} , $\log g$, metallicity, E(B-V), radius, luminosity and mass from the low resolution spectra and HST photometry, in section 3. Section 4 presents the results of the analysis together with a discussion of their uncertainties. The metallicity of NGC 300 obtained from this work is discussed in section 5 and compared with previous work. Section 6 investigates stellar properties and evolutionary time scales. The new FGLR is presented in section 7 together with a detailed discussion of the uncertainties. Conclusions and outlook towards future work are given in section 8.

2. Observations

The spectroscopic observations were obtained with FORS1 at the ESO VLT in multiobject spectroscopy mode in two consecutive nights of excellent seeing conditions (typical 0.7 arcsec, but long spells of 0.4 to 0.5 arcsec) on 2000 September 25 and 26 as part of the Auracaria Project (Gieren et al. (2005b)). Four fields (A, B, C, D) were observed in five exposures, each lasting 45 minutes. The spectral resolution is approximately 5 Å and the spectral coverage extends from shortward of the Balmer jump to $H\beta$ or beyond for most of our targets. The observational data set has been described by Bresolin et al. (2002). The paper also contains finding charts, coordinates, photometry (ESO/MPI 2.2m WFI) and spectral types. Of the 62 confirmed supergiants found with spectral types ranging from late O to F, 29 were of spectral type B8 to A5 - the spectral type of interest for this study - and were not severely contaminated by HII emission or composite (indicating a contribution of a star of different spectral type). 24 of those had a S/N per pixel of about 40 or better, sufficient for our quantitative analysis. This is the sample listed in Table 1 and selected for the work presented in the following. The target designation is the same as in Bresolin et al. (2002). Note that a quantitative spectral analysis of the early type B supergiants

(spectral type B0 to B3) has already been published by Urbaneja et al. (2005).

The analysis method presented in the next section makes use of the strength of the observed Balmer jump D_B . (Fortunately, FORS was developed with high UV throughput as a design goal, which turns out to be an enormous advantage for our study). To measure D_B we selected one 45 minute exposure for each of the observed fields (usually the exposure with the best seeing) and used standard stars to obtain a flux calibration of our spectra, where special care was given to the calibration in the near UV. While the single exposures are somewhat noisy, they do allow for a rather accurate measurement of D_B (see next section). Slit losses due to the 1 arcsec slitlets can be corrected for by renormalizing the observed flux calibrated spectrum to the HST B-band photometry. They are unimportant to first order, since D_B is a relative measurement of fluxes shortward and longward of 3647 Å. However, we have to worry about second order effects caused by the wavelength dependence of seeing and resulting wavelength dependent slit losses. Fortunately, FORS is equipped with an atmospheric dispersion compensator, which was used for our observations, thus, already correcting for slit losses caused by atmospheric dispersion. The effects of wavelength dependent seeing were addressed in the following way. We measured the FWHM of our spectra on the detector perpendicular to the direction of dispersion as a function of wavelength. This provided us with an estimate of the seeing as a function of wavelength. Assuming a Moffat-function (with exponent $\beta = 2$) for the PSF we were then able to calculate slit-losses at every wavelength from the measured seeing FWHM using the simple formulae

$$\begin{aligned} PSF(\phi) &\propto 1/\{1 + (\phi/\alpha)^2\}^\beta \\ F_\lambda^{new} &= F_\lambda^{old}(1 + (\alpha/w)^2)^{0.5} \\ \alpha &= 0.7769FWHM(\lambda) \end{aligned} \tag{1}$$

w is the slit half-width corresponding to 0.5 arcsec.

The relative flux corrections obtained in this way are small over the wavelength range, which we use for measuring or fitting the Balmer jump D_B (3585 Å to 3876 Å). The logarithm of ratio of the correction factors at these two wavelength are 0.016, 0.070, 0.024 and 0.004 for fields A, B, C, D respectively, smaller or comparable to the stochastic errors caused by the photon noise. Assuming a Moffat-function with $\beta = 3$ yields very similar results.

The original photometry for our targets was obtained with the ESO 2.2m and the Wide Field Imager as a result of a multiepoch survey for Cepheids (Bresolin et al. 2002). Bresolin et al. (2004) have used these data for a study of blue supergiant photometric variability. No significant variability has been found for our targets.

Almost all of our targets were observed with HST/ACS in an investigation of the effects of blending on the Cepheid distance to NGC 300 (Bresolin et al. 2005), which were found to

be negligible. With A supergiants being significantly brighter than Cepheids it is obvious that blending and multiplicity should not be an issue for this study, as is also confirmed by a comparison of the ground-based and HST/ACS V and I photometry. Bresolin et al. (2005) detected an offset of 0.1 mag between ESO/WFI and HST/ACS B-band photometry, which they attributed to a calibration uncertainty of the ground-based data. We will use the HST/ACS photometry for our targets, where available. For three objects, we do not have HST data. In these cases, we use the ESO/WFI B, V, I data but apply a 0.1 mag correction to the B-band.

3. Analysis Method

For the quantitative analysis of the spectra we will use the same combination of line blanketed model atmospheres and very detailed NLTE line formation calculations as Przybilla et al. (2006) in their high signal-to-noise and high spectral resolution study of galactic A-supergiants. The model atmosphere assumptions and the individual atomic models used for the NLTE calculations have been described in this paper, which also contains a variety of tests with regard to the accuracy and consistency that can be obtained. In the spectral range to be used in our work (3500 Å to 5500 Å) these calculations reproduce the observed normalized spectra and the spectral energy distribution, including the Balmer jump, extremely well. For the four objects studied, Przybilla et al. (2006) calculated a relatively small grid of models centered around the expected parameters for each star followed by more line formation calculations to obtain element abundances, once the stellar parameters were determined. The large sample of 24 objects in our study requires a different approach. We calculate an extensive, comprehensive and dense grid of model atmospheres and NLTE line formation covering the potential full parameter range of all the objects in gravity, effective temperature and metallicity. We then use the synthetic spectra and energy distributions obtained in this multi-dimensional parameter space to constrain the stellar parameters. The gravities and temperatures of the grid are displayed in Fig. 1.

At each grid point we have a set of models with line formation calculations for the following metallicities $[Z] = \log Z/Z_{\odot}$: -1.30, -1.00, -0.85, -0.70, -0.60, -0.50, -0.40, -0.30, -0.15, 0.00, 0.15, 0.30. Z/Z_{\odot} is the metallicity relative to the sun in a sense that the abundance for each element is scaled by the same factor relative to its solar abundance. Solar abundances were taken from Grevesse & Sauval (1998). We note that by scaling abundances in this way we are not able to detect deviations from the solar abundance pattern but only general changes in metallicity. We are confident that it will be possible to extend this work to at least a study of the relative ratio of α - to iron-group elements as a function of galactocentric distance. But at this stage we restrict our work to a discussion of stellar metallicities and the metallicity gradient and postpone a more detailed study to follow-up work.

A determination of metallicities always requires an estimate of the photospheric microturbulence velocity v_t normally obtained from the constraint that weak and strong lines of each ion should yield the same element abundance. At our spectral resolution it is difficult to constrain microturbulence in this way, thus, we rely on the results of the high resolution work done for A supergiants in the Milky Way and Local Group galaxies, which, fortunately, shows a very consistent pattern of v_t as a function of stellar gravities (Przybilla 2002, Przybilla et al. 2006, Venn 1995a, Venn 1995b, Venn et al. 2000, Venn et al. 2001, Venn et al. 2003, Kaufer et al. 2004). At low gravities the values of v_t are about 8 km/sec and decrease to lower values of about 4 km/sec at higher gravities. The values of v_t adopted for this study, accordingly, are also displayed in Fig. 1.

The analysis of the each of the 24 targets proceeds in three steps. First, the stellar parameters (T_{eff} and $\log g$) are determined together with interstellar reddening and extinction, then the metallicity is determined and finally, assuming a distance to NGC 300, we obtain stellar radii, luminosities and masses. For the first step, a well established method to obtain the stellar parameters of supergiants of late B to early A spectral type is to use ionization equilibria of weak metal lines (OI/II; MgI/II; NI/II etc.) for the determination of effective temperature T_{eff} and the Balmer lines for the gravities $\log g$. The most recent high resolution work cited in section 1 has very convincingly shown that very accurate results can be obtained in this way, when detailed non-LTE line formation calculations are used. However, at the low resolution of 5 Å the weak spectral lines of the neutral species disappear in the noise of the spectra and an alternative technique is required to obtain temperature information.

One simple way is to use the information from stronger lines in the spectrum which define the spectral type and then to apply a spectral type - temperature calibration based on the high resolution quantitative spectroscopic work. This technique was used by Bresolin et al. (2001), Bresolin et al. (2002) and Kudritzki, Bresolin & Przybilla (2003). The disadvantage of this method is obvious. As soon as the metallicity of the objects investigated with this low resolution method is significantly different from the metallicity of the objects which are used to calibrate the spectral type effective temperature relationship, substantial errors can be introduced. For instance, objects at a lower metallicity will have weaker characteristic metal lines and will thus be assigned a spectral type earlier than an object of the same effective temperature but higher metallicity. Thus, without a priori knowledge of the metallicity this method might indeed introduce large uncertainties. Evans & Howarth (2003) have investigated this effect for A supergiant of luminosity class II in the Magellanic Clouds by studying the CaII lines and found significant effects. However, our targets are more luminous (luminosity class I) and the spectral type classification used in the papers mentioned above did not use the CaII lines, but the metal line spectrum in the range from 4400 to 4700 Å. Thus, an extended investigation is needed.

Fortunately, the comprehensive model atmosphere and line formation grid described above

makes it easy to investigate the degeneracy of the metal line spectrum with temperature and metallicity. All we have to do is to follow the isocontours of constant Balmer line equivalent widths in the $(\log g, \log T_{\text{eff}})$ plane (see Fig. 5) (along which the Balmer lines as a gravity indicators have identical profiles at 5 Å resolution) and to compare synthetic metal line spectra of models with different T_{eff} and $[Z]$. A rather dramatic example obtained in this way is shown in Fig. 2 with metal line spectra of three models at different pairs of T_{eff} and $\log g$, where the Balmer line profiles are exactly the same. The models have different metallicity $[Z]$. The hottest model at $T_{\text{eff}} = 10500$ K with a metallicity slightly higher than solar ($[Z] = 0.15$) has an almost identical metal line spectrum as the coolest model at $T_{\text{eff}} = 8750$ K with a metallicity significantly lower than solar ($[Z] = -0.50$).

Thus, while all three models have exactly the same Balmer line profiles and would fit the observed Balmer lines of a hypothetical star to be analyzed, we would have a hard time to independently determine temperature and metallicity from the rest of the spectrum, which looks very similar for all three models. Fortunately, the strength of HeI λ 4471 allows, in principle, to distinguish between the hottest model and the two cooler ones, and this will be one of the alternative techniques that we will use in the following. However, it seems impossible to extract the temperature difference between the two cooler models from the spectra displayed. We note the slightly enhanced strengths of the TiII lines at low temperature, but using these lines as an independent temperature indicator while simultaneously fitting the Balmer lines would be based on an assumption on the abundance ratio of titanium to iron, and, thus, the ratio of α -elements to iron-group elements. While the investigation of the possible variation of the ratio as a function of galaxy evolution, is beyond the scope of this paper (see above), it will certainly become important in future work. We, thus, need a temperature indicator independent from any a priori assumptions about general metallicity and relative abundance ratios of metals. This is in particular important, as the spiral galaxies, which we intend to investigate with our spectroscopic technique, are assumed to have significant metallicity gradients and possibly also gradients, for instance, in their α to iron-group element ratios.

A very obvious way out of this dilemma is the use of the spectral energy distributions (SEDs) and here, in particular of the Balmer jump D_B . Fig. 3 and 4 show, how the degeneracy of the temperature vs. metallicity diagnostic is broken. Very obviously, the SEDs and D_B 's of the three models with almost identical metal line spectra are significantly different. While the observed photometry from B-band to I-band will be used to constrain the interstellar reddening, we can use D_B as a temperature diagnostic. For stars of spectral type A this idea is certainly not new and goes back to the classical work by Chalonge and Divan in the 1950's. For A supergiants it has been successfully investigated and applied by Groth (1961), Aydin (1972), and Kudritzki (1973).

The basis for our diagnostic technique is given in Fig. 5. It shows isocontours of constant H δ equivalent width and of constant values of the Balmer jump D_B . The Balmer jump is defined as

below

$$\begin{aligned}
 D_B &= \langle \log(F_\lambda^{long}) \rangle - \langle \log(F_\lambda^{short}) \rangle \\
 \langle \log(F_\lambda^{long}) \rangle &= \{ \log F_{3782\text{\AA}}^\circ + \log F_{3814\text{\AA}}^\circ + \log F_{3847\text{\AA}}^\circ + \log F_{3876\text{\AA}}^\circ \} / 4 \\
 \langle \log(F_\lambda^{short}) \rangle &= \{ \sum_{i=1}^N \log(F_{\lambda_i}) \} / N, \quad 3585\text{\AA} \leq \lambda_i \leq 3627\text{\AA}
 \end{aligned} \tag{2}$$

The wavelengths for the individual fluxes on the longward side are selected to avoid the wings of the Balmer lines and stronger metal line features. In this definition, the dependence of D_B on $[Z]$ is very weak and can be neglected, as an inspection of our model grid shows. The same is true for the strengths of the Balmer lines and, thus, the diagnostic diagram of Fig. 5 is metallicity independent. While the two sets of isocontours are not perfectly orthogonal, they certainly lead to well defined intersection points except very close to the Eddington-limit.

3.1. Effective temperature, Gravity and Reddening

Guided by Fig. 5 we apply the following diagnostic technique to determine effective temperature and gravity. We use the normalized spectra of our targets to interactively fit the Balmer lines profiles H_{10} to H_γ with our model spectra grid in the $(\log g, \log T_{eff})$ plane (the fit curves obtained in this way follow very closely the isocontours of Balmer lines as in the example of Fig. 5). Then, we fit the observed SED and the Balmer jump in the same diagnostic plane. Our multi-color photometry from B-band to I-band compared with the model fluxes allows to determine reddening and extinction and the calibrated FORS fluxes around the Balmer jump (see section 2) fitted with the model fluxes yield a second fit curve for D_B (again very similar to the isocontours in Fig. 5). The intersection of the two fit curves defines temperature and gravity.

An example is given in Figs. 6, 7, and 8 for object No. 21 of our sample. At a fixed value of effective temperature the Balmer lines allow for a determination of $\log g$ within 0.05 dex uncertainty. The uncertainty of Balmer jump D_B measured from the SED fit can be (conservatively) estimated to be 0.02 dex corresponding to a temperature uncertainty ${}^{+200}_{-150}\text{K}$ at the fixed gravity of 1.55 at $T_{eff} = 10000$ K. (The values of D_B obtained from SED fit are given in Table 1). Applying the same fit procedure at different effective temperatures in the $(\log g, \log T_{eff})$ plane leads to the fit diagram of Fig. 8. While the uncertainties at a fixed pair of T_{eff} and $\log g$ are rather small, the fact that the two sets of fit curves for the Balmer lines and the Balmer jump are not orthogonal leads to the significantly larger error box, which is obtained from the intersection of the dashed curves. The uncertainty of our low resolution analysis obtained in this way are ${}^{+600}_{-470}\text{K}$ for T_{eff} and ${}^{+0.19}_{-0.17}$ dex for $\log g$, respectively. This is roughly a factor of two larger than what can be obtained

with high quality, high resolution spectra and the use of ionization equilibria from weak lines (see Przybilla et al. 2006) but still good enough to determine metallicities $[Z]$ with a reasonable accuracy, as we will demonstrate below. The fit of T_{eff} and $\log g$ also yields the value of interstellar reddening $E(B-V) = 0.13$ mag from a comparison of computed model fluxes with fluxes obtained from HST photometry (see Bresolin et al. 2004 for the photometric data). As for the calculation of the reddening law we use the formulae given by Cardelli et al. (1989) and $R_V = 3.1$ for the ratio of visual extinction A_V and reddening $E(B-V)$.

The accurate determination of T_{eff} and $\log g$ is crucial for the use of A supergiants as distance indicators using the relationship between absolute bolometric magnitude M_{bol} and flux weighted gravity $\log g_F$ defined as

$$\log g_F = \log g - 4\log T_{eff,4} \quad (3)$$

where $T_{eff,4} = T_{eff}/10000K$ (see Kudritzki, Bresolin & Przybilla 2003). The relatively large uncertainties obtained with our fit method may cast doubts whether $\log g_F$ can be obtained accurately enough. Fortunately, the non-orthogonal behaviour of the fit curves in Fig. 8 leads to errors in T_{eff} and $\log g$, which are correlated in a way that reduces the uncertainties of $\log g_F$. This is demonstrated in Fig. 9, which shows the corresponding fit curves of the Balmer lines and D_B in the $(\log g, \log T_{eff})$ plane. We obtain much smaller uncertainties of $\log g_F$ for target No. 21, namely $^{+0.09}_{-0.08}$. We will discuss the physical reason behind this in section 6.

We have applied this diagnostic technique on all targets, for which we were able to obtain observations of the Balmer jump. In two cases (target No. 0 and 10), the set-up of the FORS slitlets did not allow to obtain spectral information shortward of the Balmer edge. For those, we use the strong temperature dependence of the observed HeI lines to constrain T_{eff} (see Fig. 2). For targets No. 2 and 4 we have used the observed HeI lines as an additional temperature criterium, since for both of them the intersections of the D_B and Balmer line fit curves are not well defined. The errors in T_{eff} obtained in these four cases are comparable to those obtained with the Balmer jump for most of the other stars. The HeI lines provide a very useful alternative diagnostic tool, however this technique works only at high enough temperatures and low gravities. The results for T_{eff} , $\log g$, $\log g_F$ and $E(B-V)$ for all targets are summarized in Table 1.

Generally, the uncertainties for T_{eff} , $\log g$, and $\log g_F$ are similar to those obtained for our example target. However, for the effective temperature errors $\Delta T_{eff}/T_{eff}$ there is a slight trend with temperature as shown by Fig. 10, which comes from the fact that the Balmer jump becomes less temperature dependent at higher temperatures (see Fig. 5). On average, temperatures are accurate to 5 percent. This is an uncertainty roughly twice as large as for the analysis of high resolution and high S/N spectra of similar objects (see Przybilla et al. 2006). The uncertainties for gravities and

flux weighted gravities are 0.2 dex and 0.1 dex on average, again twice as large as for the analysis of high quality spectra. This is a result of the larger uncertainty of the temperature determination.

3.2. Metallicity

Knowing the stellar atmospheric parameters T_{eff} and $\log g$ we are able to determine stellar metallicities by fitting the metal lines with our comprehensive grid of line formation calculations. The fit procedure proceeds in several steps. First, we define spectral windows, for which a good definition of the continuum is possible and which are relatively undisturbed by flaws in the spectrum (for instance caused by cosmic events) or interstellar emission and absorption. A typical spectral window used for all of our targets is the wavelength interval $4497 \text{ \AA} \leq \lambda \leq 4607 \text{ \AA}$. Fig. 11 shows the synthetic spectrum calculated for the atmospheric parameters of target No. 21 (the example of the previous subsection) and for all the metallicities of our grid ranging from $-1.30 \leq [Z] \leq 0.30$. It is very obvious that the strengths of the metal line features are a strong function of metallicity. In Fig. 12 we show the observed spectrum of target No. 21 in this spectral region overplotted by the synthetic spectrum for each metallicity. We use separate plots for each metallicity, because the optimal relative normalization of the observed and calculated spectra is obviously metallicity dependent. We address this problem by renormalizing the observed spectrum for each metallicity so that the synthetic spectrum always intersects the observations at the same value at the two edges of the spectral window (indicated by the dashed vertical lines). The scaling of the observed spectrum between the two edges is done by a simple linear interpolation. The next step is a pixel-by-pixel comparison of calculated and normalized observed fluxes for each metallicity.

$$(O - C)^2([Z])_i = \left[\sum_{j=1}^{n_{pix}} (F([Z])_j^{obs} - F([Z])_j^{calc})^2 \right] / n_{pix} \quad (4)$$

The index i refers to spectral window selected. If we define

$$\chi([Z])_i = S/N * (O - C)([Z])_i, \quad (5)$$

where S/N is the signal-to-noise ration per resolution element, we can look for the minimum $\chi([Z])_i$ as a function of $[Z]$ to determine metallicity. This is done in Fig. 13, which yields $[Z] = -0.40$. Application of the same method on different spectral windows provides additional independent information on metallicity as shown in Fig. 14 and 15. The average metallicity obtained from all windows is $[Z] = -0.39$ with a very small dispersion of only 0.02 dex.

While it seems that our method yields a very accurate metallicity for a fixed pair of stellar

parameters T_{eff} and $\log g$, we also need to consider the effect of the stellar parameter uncertainties on the metallicity determination. This is done by applying the same correlation method for $[Z]$ for models at the extremes of the error box for T_{eff} and $\log g$, as given by Fig. 8 and Table 1. This increases the uncertainty of $[Z]$ to ± 0.15 dex.

We apply the same method to all the objects of our sample. The results are given in Table 1. In some case the uncertainties are larger than for target No. 21, which is caused by larger uncertainties of the atmospheric parameters or more noise in the spectra or both.

3.3. Radii, Luminosities and Masses

The fit of the observed photometric fluxes with the model atmosphere fluxes was used to determine interstellar reddening $E(B-V)$ and extinction $A_V = 3.1 E(B-V)$. Simultaneously, the fit also yields the stellar angular diameter, which provides the stellar radius, if a distance is adopted. Alternatively, for the stellar parameters (T_{eff} , $\log g$, $[Z]$) determined through the spectral analysis the model atmospheres also yield bolometric corrections BC, which we use to determine bolometric magnitudes. These bolometric magnitudes then also allow us to compute radii. The radii determined with these two different methods agree within a few percent. We have chosen the latter method for the radii given in Table 2. Gieren et al. (2005a) in their multi-wavelength study of a large sample of Cepheids in NGC 300 including the near-IR have determined a new distance modulus $m-M = 26.37$ mag, which corresponds to a distance of 1.88 Mpc. We have adopted these values to obtain the radii and absolute magnitudes in Table 2.

In the temperature range of $8300 \text{ K} \leq 12000 \text{ K}$ of our model grid (see Fig. 1) the individual BC-values of the models are well represented by an analytical fit formula

$$BC(T_{eff}, \log g, [Z]) = f(\log g_F) - 4.3 \log T_4(1 + \log T_4) + D_Z \quad (6)$$

where $T_4 = T_{eff}/10000 \text{ K}$ and

$$D_Z = 0.09[Z](1 + 0.26[Z]) \quad (7)$$

$$f(\log g_F) = f_{max}(1 - a \exp(-(\log g_F - x_{min})/h))$$

and $a = 1 - f_{min}/f_{max}$, $f_{min} = -0.39$, $f_{max} = -0.265$, $x_{min} = 1.075$, $h=0.17$. The fit is accurate to 0.02 mag over the whole range of model parameters. It allows us to estimate the uncertainties of bolometric magnitudes arising from the uncertainties of the stellar parameters. The errors for M_{bol} given in Table 2 include these uncertainties together with the photometric errors.

We note that in most cases fit formulae provided for bolometric corrections do not include the effects of gravity. In the case of A supergiants this would lead to significant error residuals of the fit of the order of 0.4 mag. Thus, the inclusion of the function $f(\log g_F)$ is essential for the expression of BC.

In our model atmosphere approach to calculate bolometric corrections we convert the model flux at the V-band effective wavelength into a V-magnitude in the usual way using a constant, which transforms the flux of Vega into the Vega V-magnitude. We then use the integral over the total model spectral energy distribution and the effective temperature of the Sun (5777K) to calculate the bolometric magnitude (assuming $M_{bol}^{\odot} = 4.74$ mag). The difference between the bolometric and the V-magnitudes calculated in this way then yields the bolometric correction. This approach provides the correct bolometric correction for Vega, which is exactly in the effective temperature range of the objects we are dealing with. We have, therefore, decided not to re-normalize our BC values to avoid small positive values at low effective temperatures, as has been suggested by Buser & Kurucz (1978) (but see also the full discussion on this matter in this paper). As a result, our BC-values are about 0.12 mag larger than the ones given by Przybilla et al. (2006), who have used the approach by Buser & Kurucz (1978).

There are two ways to determine stellar masses. We can use the stellar gravities together with the radii to directly calculate masses. We call the masses derived in this way spectroscopic masses. Alternatively, masses can be estimated by comparing the location of our target stars in the HRD with evolutionary tracks (Meynet & Maeder 2005). Masses obtained in such a way are called evolutionary masses. Both values are given in Table 2 for each target star. The uncertainties are discussed in section 4.2.

4. Results

In this section we discuss the main results of our quantitative spectral analysis.

4.1. Interstellar Reddening

Our quantitative spectroscopic method yields interstellar reddening and extinction as a by-product of the analysis process. For objects embedded in the dusty disk of a star forming spiral galaxy we expect a wide range of interstellar reddening $E(B-V)$. Indeed, we find a range from $E(B-V) = 0.07$ mag up to 0.24 mag. Fig. 16 shows the distribution of interstellar reddening among the 24 stars of our sample. The individual reddening values are significantly larger than the value of 0.03 mag adopted in the HST distance scale key project study of Cepheids by Freedman et al. (2001) and

demonstrates the need for a reliable reddening determination for stellar distance indicators, at least as long the study is restricted to optical wavelengths. The average over our sample is $\langle E(B - V) \rangle = 0.12$ mag in close agreement with the value of 0.1 mag found by Gieren et al. (2005a) in their optical to near-IR study of Cepheids in NGC 300. While Cepheids have somewhat lower masses than the A supergiants of our study and are consequently somewhat older, they nonetheless belong to the same population and are found at similar sites. Thus, we expect them to be affected by interstellar reddening in the same way as A supergiants.

4.2. Stellar properties

The original motivation for the development of our analysis technique using the Balmer jump was the degeneracy between the effective temperature derived from the spectral type and metallicity. In Fig. 17 and 18 we compare the temperatures obtained with the two different methods. We use the compilation by Kudritzki, Bresolin & Przybilla (2003) for the relationship between spectral type and effective temperature. While there is a clear correlation between the two temperatures, there is definitely a shift to higher temperatures for $T_{eff}(\text{spectral type})$, which is explained by the fact that all of our targets have a metallicity smaller than in the solar neighborhood. Fig. 19 indicates that the effect becomes larger with decreasing metallicity, exactly as expected (for the discussion of metallicities we refer to the next section).

Fig. 20 shows the location of our targets in the $(\log g, \log T_{eff})$ plane compared to the early B-supergiants studied by Urbaneja et al. (2005). The comparison with evolutionary tracks (Meynet & Maeder 2005) gives a first indication of the stellar masses in a range from $10 M_{\odot}$ to $40 M_{\odot}$. Three targets have obviously higher masses than the rest of the sample and seem to be on a similar evolutionary track as the objects studied by Urbaneja et al. (2005).

An alternative way to discuss the evolutionary status of our targets is the classical HRD. This is done in Fig. 21. The evolutionary information obtained from this diagram compared with Fig. 20 appears to be consistent. The B-supergiants seem to be more massive than most of the A supergiants. The same three A supergiants apparently more massive than the rest in Fig. 20 are also the most luminous objects in Fig. 21. This confirms that quantitative spectroscopy is -at least qualitatively - capable to retrieve the information about absolute luminosities. Note that the fact that all the B supergiants studied by Urbaneja et al. (2005) are more massive is simply a selection effect of the V magnitude limited spectroscopic survey by Bresolin et al. (2002). At similar V magnitude as the A supergiants those objects have higher bolometric corrections because of their higher effective temperatures and are, therefore, more luminous and massive.

The luminosity uncertainties for our targets range from 0.02 dex to 0.06 dex (the latter rather

large errors appear only in a few rare cases, see Table 2). Correspondingly, Fig. 21 allows to determine stellar masses based on evolutionary tracks with a much better resolution than Fig. 20. We have used the evolutionary tracks by Meynet & Maeder (2005) (and references therein) to construct mass luminosity relationships in the A supergiant stage of the form

$$\log L/L_{\odot} = (a - bx)x + c, \quad x = \log M/M_{\odot} - \log M^{min}/M_{\odot} \quad (8)$$

The coefficients for different evolutionary models (with and without rotation, Milky Way and SMC metallicity) are given in Table 4. The fit reproduces model masses for a given luminosity (in the range $-6.5 \geq M_{bol} \geq -9.7$) to better than 5% or 0.02 dex. With the bolometric magnitudes in Table 2 we can then determine evolutionary masses, which are also given in Table 2. We have chosen the mass-luminosity relationship for tracks with rotation and SMC abundance, the other relationships give similar results. The reason why we selected Milky Way and SMC metallicities as a representative grid of evolutionary tracks is that only for those a complete set of tracks is available.

With the small errors in luminosity, we obtain masses which formally have very small uncertainties of at most 5%. However, the masses are, of course, affected by the systematic uncertainties of the evolutionary tracks through the effects of mass-loss, rotation, mixing and opacity. One particular problem may arise through blue loops from the red giant branch (RGB) or crossing to the blue from the RGB. Fortunately, for the mass and luminosity range of interest ($12M_{\odot} \leq M \leq 30M_{\odot}$, $-6.5 \leq M_{bol} \leq -9.3$) we find that the published tracks (in particular at lower metallicity) do not show significant loops or second crossings.

An alternative way to determine masses is, of course, to use directly the stellar gravities and radii determined through the fitting of stellar spectra and SEDs. These spectroscopic masses are also given in Table 2. Note that we have not included the effects of centrifugal forces on the effective stellar gravities to derive spectroscopic masses. While this is important for O-stars (see Repolust et al. 2004), the rotational velocities of A supergiants (~ 30 km/s) are too small and the radii too large to cause an effect. Fig. 22 and 23 compare the masses derived by the two different methods. Given the fact that uncertainties of the spectroscopic masses are roughly as large as the gravity uncertainties (0.1 to 0.2 dex) the comparison is generally encouraging. At the high mass end, we have agreement within the uncertainties. At the low mass end, however, the evolutionary masses seem to be somewhat higher on average. There is the indication of a trend of this effect to become stronger with decreasing spectroscopic mass. At this point, we have no explanation for this result. If it is not an artefact of the spectroscopic technique applied, then it may indicate that the effects of blue loops are more important than the evolutionary models available to us predict. Blue loops increase the luminosity at a given mass (at the low mass end the amount of mass-loss is still small at the RGB), thus, their neglect would lead to an overestimate of the evolutionary mass.

The most extreme object in the left part of Figures 22 and 23 is target No. 17 of Tables 1 and 2. It is the object with the lowest luminosity in the HRD (Fig. 21) corresponding to a mass of $11 M_{\odot}$. Its position in the $(\log g, \log T_{\text{eff}})$ plane of Fig. 20 is right on the track with an initial mass of $15 M_{\odot}$, but with the low gravity determined through spectroscopy its radius is too small to yield mass high enough in comparison with the evolutionary mass.

4.3. Metallicity Gradient

The metallicities of the individual targets together with their galacto-centric distance are given in Table 1 and allow us to discuss the stellar metallicity and the metallicity gradient in NGC 300. Fig. 24 shows the stellar metallicities $[Z]$ as function of galactocentric distance, expressed in terms of the isophotal radius, ρ/ρ_0 . Despite the scatter caused by the metallicity uncertainties of the individual stars the metallicity gradient of the young disk population in NGC 300 is very clearly visible. A linear regression (excluding target No. 1, the outlier at $\rho/\rho_0 = 0.81$ and $[Z] = -0.04$) for the combined A- and B-supergiant sample yields

$$[Z] = -0.06 \pm 0.09 - 0.44 \pm 0.12 \rho/\rho_0 \quad (9)$$

for the angular gradient. On a linear scale (d in kpc) we obtain

$$[Z] = -0.06 \pm 0.09 - 0.083 \pm 0.022 d. \quad (10)$$

We obtain a very similar regression, if we restrict the sample to A-supergiants only, which indicates that there is no systematic abundance difference between these two groups of stars. Our new result confirms the result obtained by Urbaneja et al. (2005), but with a much larger sample the metallicity gradient and the zero point are now much better defined. Note that the metallicities of the B supergiants refer to oxygen only with a value of $\log[N(\text{O})/N(\text{H})] = -3.31$ adopted for the sun (Allende Prieto, Lambert & Asplund 2001). On the other hand, the A supergiant metallicities reflect the abundances of a variety of heavy elements such as Ti, Fe, Cr, Si, S, and Mg.

With this result we can resume the discussion started by Urbaneja et al. (2005) and compare with oxygen abundances obtained from HII-region emission lines. Urbaneja et al. (2005) used line fluxes published by Deharveng et al. (1988) and applied various different published strong line method calibrations to determine nebular oxygen abundances, which could then be used to obtain the similar regressions as above. The results for zero points and gradients compared to our work are given in Table 3 (for a discussion of the individual calibrations we refer to Urbaneja et al. 2005).

The different strong line method calibrations lead to significant differences in the central metallicity as well as in the abundance gradient. The calibrations by Dopita & Evans. (1986) and Zaritsky et al. (1994) predict a metallicity significantly supersolar in the center of NGC 300 contrary to the other calibrations. Our work yields a central metallicity slightly smaller than solar in good agreement with Denicolo et al. (2002) and marginally agreeing with Kobulnicky et al. (1999), Pilyugin (2001), and Pettini & Pagel (2004). At the isophotal radius, 5.3 kpc away from the center of NGC 300, we obtain an average metallicity significantly smaller than solar $[Z] = -0.50$, close to the average metallicity in the SMC. The calibrations by Dopita & Evans. (1986), Zaritsky et al. (1994), Kobulnicky et al. (1999) do not reach these small values for oxygen in the HII regions either because their central metallicity values are too high or the metallicity are gradients too shallow.

In light of the substantial range of metallicities obtained from HII region emission lines using different strong line method calibrations it seems to be extremely valuable to have an independent method using young stars. It will be very important to compare our results with advanced work on HII regions, which will avoid strong line methods, and will use direct information about nebular electron temperatures and densities (Bresolin et al., 2008, in preparation).

As mentioned before, there is a suspicious outlier in Fig. 24. We have checked the stellar parameters and metallicity of this object several times and have not found a reason to discard the high metallicity value found, which is 0.38 dex above the average value at this galacto-centric distance. A similar example is target No.14 at the largest galacto-centric distance. While we cannot exclude that something went wrong in the analysis, we also want to state very firmly that the expectation of homogeneous azimuthal metallicity in patchy star forming spiral galaxies seems naive to us. The continuation of this type of work on other galaxies will show whether cases like this are common or not. We note that the high resolution spectral analysis of A supergiants in WLM by Venn et al. (2003) has detected a similar outlier case.

So far, we have only tried to determine an average metallicity $[Z]$ for each star. Together with the challenge of an accurate determination of stellar parameters we felt that this was a good first reasonable step to obtain quantitative information from our low resolution spectra. While $[Z]$ in the way how our method works is mostly determined by an overlap of Fe, Ti and Cr lines, we have also observed that certain spectral windows are dominated by a majority of lines of specific element species. In future work we will try to use this observation to determine relative fractions of abundances of α - elements such as Mg and Ti to iron-group elements such as Fe and Cr. It will be an important goal to investigate whether this ratio is constant or not as a function of galactocentric distance.

5. Stellar Properties and Evolutionary Lifetimes

The progenitor stars of the A supergiants of our sample were obviously O-stars in a mass range between 15 to 25 M_{\odot} . The HST/ACS photometry of Bresolin et al. (2005) allows to estimate how many of such progenitor stars are present in exactly the same field. Fig. 25 shows the corresponding combined color-magnitude diagram. Adopting our mean reddening of $E(B-V) = 0.12$ together with the corresponding mean visual extinction of $A_V = 0.37$, a distance modulus of 26.37 mag, an absolute magnitude of $M_V = -2.7$ mag for a 15 M_{\odot} star on the zero age main sequence, we can assume that all stars brighter than $m_V = 24.0$ mag are possible progenitors of A supergiants. Fig. 26 shows the number of star counts in our fields in bins of 0.1 mag as a function of magnitude. The curve is well fitted by

$$\log n = a_{\star} m_V + b_{\star} \quad (11)$$

and $a_{\star} = 0.5622$, $b_{\star} = -9.921$ (see also Bresolin et al. 1996, Bresolin et al. 1998). While the number of star counts starts to become incomplete at $m_V = 21.5$ mag we can extrapolate the fit to calculate the total cumulative number N of stars down to $m_V = 24.0$. We obtain $N = 2.9 \times 10^4$ for the present number of progenitor stars. Assuming continuous star formation and having 24 confirmed A supergiants in the fields the ratio $24/2.9 \times 10^4 = 8.3 \times 10^{-4}$ provides a lower limit for the evolutionary lifetime in the A supergiant stage in units of the main sequence lifetime.

The total number of A supergiants in the observed fields in the mass range between 15 to 25 M_{\odot} can then be estimated from Bresolin et al. (2002), who found a total of 167 supergiant candidates in the combined color magnitude diagram. They obtained spectra for 70 of those and detected 29 A supergiants, i.e. a fraction of 41%. Assuming the same fraction for the original total of 167 candidates leaves us with an estimate of 69 A supergiants. The observed ratio of evolutionary lifetime in the A supergiant stage to the main sequence lifetime is then $69/2.9 \times 10^4 = 2.4 \times 10^{-3}$.

The corresponding lifetime ratio for evolutionary tracks is a strong function of metallicity. Comparing calculations including the effects of rotation (Meynet & Maeder 2005) we obtain 2×10^{-2} for SMC metallicity and $2 - 8 \times 10^{-4}$ for Milky Way metallicity. With metallicities for most of our target stars between these extremes we conclude that our empirical lifetime estimate agrees with the prediction of the evolutionary models.

6. Flux Weighted Gravity - Luminosity Relationship (FGLR)

As discussed in the previous sections, massive stars with masses in the range from $12 M_{\odot}$ to $40 M_{\odot}$ evolve through the B and A supergiant stage at roughly constant luminosity (see Fig. 21). In addition, since the evolutionary timescale is very short when crossing through the B and A supergiant domain, the amount of mass lost in this stage is small. This means that the evolution proceeds at constant mass and constant luminosity. This has a very simple, but very important consequence for the relationship of gravity and effective temperature along each evolutionary track. From

$$L \propto R^2 T_{\text{eff}}^4 = \text{const.}; M = \text{const.} \quad (12)$$

follows immediately that

$$M \propto g R^2 \propto L (g/T_{\text{eff}}^4) = L g_F = \text{const.} \quad (13)$$

Thus, along the evolution through the B and A supergiant domain the “*flux-weighted gravity*” $g_F = g/T_{\text{eff}}^4$ should remain constant. This means each evolutionary track of different luminosity in this domain is characterized by a specific value of g_F . This value is determined by the relationship between stellar mass and luminosity, which in a first approximation is a power law

$$L \propto M^x . \quad (14)$$

We note from section 4.2 that the mass-luminosity relationship has higher order terms, but for simplicity we use this as a first order approximation to obtain

$$L^{1-x} \propto (g/T_{\text{eff}}^4)^x . \quad (15)$$

With the definition of bolometric magnitude $M_{\text{bol}} \propto -2.5 \log L$ we then derive

$$-M_{\text{bol}} = a_{FGLR}(\log g_F - 1.5) + b_{FGLR} . \quad (16)$$

This is the “*flux-weighted gravity – luminosity relationship*” (FGLR) of blue supergiants. Note that the proportionality constant a_{FGLR} is given by the exponent of the mass – luminosity power law through

$$a_{FGLR} = 2.5x/(1-x) , \quad (17)$$

for instance, for $x = 3$, we obtain $a_{FGLR} = -3.75$. We have chosen the zero point of the relationship at a flux weighted gravity of 1.5, which is in the middle of the range encountered for blue supergiant stars.

We can use the mass-luminosity relationships of different evolutionary tracks (with and without rotation, for Milky Way and SMC metallicity) as discussed in section 4.2 and characterized by the coefficients given in Table 4 to calculate the different stellar evolution FGLRs, which are displayed in Fig. 27. Very interestingly, while different evolutionary model types yield somewhat different FGLRs, the differences are rather small. The difference is largest between the two sets of stellar evolution models for Milky Way metallicity with and without the effects of rotation. The models with SMC metallicity and rotation yield a FGLR rather close to the case with Milky way metallicity and rotation. Only at higher luminosity, where the dependence of mass-loss on metallicity starts to become important, is a larger difference from the Milky Way FGLR predicted. This is also the parameter domain, where the curvature of the FGLR becomes more significant, as to be expected from the non-linear mass-luminosity relationship of section 4.2. The set of stellar evolution models at SMC metallicity but without the effects of rotation yields a FGLR very close to the one with rotation and the same metallicity.

Kudritzki, Bresolin & Przybilla (2003) were the first to realize that the FGLR has a very interesting potential as a purely spectroscopic distance indicator, as it relates two spectroscopically well defined quantities, effective temperature and gravity, to the absolute magnitude. Compiling a large data set of spectroscopic high resolution studies of A supergiants in the Local Group and with an approximate analysis of low resolution data of a few targets in galaxies beyond the Local Group (see discussion in previous chapters) they were able to prove the existence of an observational FGLR rather similar to the theoretically predicted one.

With our improved analysis technique of low resolution spectra of A supergiants and with the much larger sample studied in our new approach we can now resume the investigation of the FGLR. We will do this in three steps. We will first discuss the determination of flux weighted gravities $\log g_F$ from the Balmer lines and will then introduce the new FGLR obtained for NGC 300. In this second step we will also include the B supergiants analyzed by Urbaneja et al. (2005). Finally, we will compare the new results obtained for NGC 300 with the previous work on Local Group A supergiants to find out whether a universal FGLR exists.

6.1. Balmer lines and Flux weighted Gravity

In Fig. 28 we show the dependence of the strength of the Balmer line H_δ characterized by its equivalent width $W_\lambda(H\delta)$ on gravity $\log g$ and effective temperature T_{eff} . Obviously, $W_\lambda(H\delta)$ de-

depends on both, gravity and temperature, and the non-horizontal isocontours displayed in Fig. 5 are the result of this dependence. The situation changes dramatically, if one looks at the dependence of $W_\lambda(\text{H}\delta)$ on flux-weighted gravity $\log g_F$ as shown in Fig. 29. Now all the curves for higher effective temperatures are on top of each other and form a temperature independent relationship, which leads to practically horizontal isocontours in the $(\log g, \log T_{\text{eff}})$ plane Fig. 30. All the other Balmer lines from H γ to H $_{10}$ show a very similar behaviour.

This has important consequences for the diagnostics of flux-weighted gravities. For objects hot enough the uncertainties of the effective temperature determination do not affect the determination of effective gravities. A simple measurement of the strengths of Balmer lines either through line profile fitting or by simply measuring the equivalent widths gives $\log g_F$ with rather high precision, as we have already pointed out in section 3.

In terms of distance determination using the FGLR this is very encouraging. It means that errors in T_{eff} stemming from the application of an inaccurate relationship between spectral types and effective temperatures caused by non-solar metallicities, as for instance in the work by Kudritzki, Bresolin & Przybilla (2003), are less important as long as the flux-weighted gravities $\log g_F$ are well determined and the objects are hot enough. Errors are only introduced through erroneous bolometric corrections and errors in E(B-V), when the observed wavelength-dependent magnitudes have to be transformed into de-reddened bolometric magnitudes. While this may still be a serious error source and should be avoided through the application of our diagnostic technique described in the previous chapters, the uncertainties of the primary quantity in the application of the method are significantly reduced increasing the reliability of the FGLR method.

Because of the importance of this effect for distance determinations we have investigated the physical reasons leading to Fig. 29 and 30. We discuss them in the remaining part of this subsection. The strength of absorption lines depends on the line strength β_V

$$\beta_V = \kappa_{\Delta V}^L / \kappa_V^c, \quad (18)$$

where $\kappa_{\Delta V}^L$ is the line absorption coefficient and κ_V^c the continuum absorption coefficient at the frequency of the line. For H δ and all other Balmer lines we have

$$\kappa_{\Delta V}^L \propto n_2 \Phi(\Delta V) \quad (19)$$

with n_2 the occupation number in the second level of hydrogen and $\Phi(\Delta V)$ the line broadening profile. Note that we have neglected the influence of stimulated emission, which is appropriate at the temperatures in question and for this qualitative discussion. For the supergiants the higher Balmer lines are always saturated in the Doppler line cores of the line profiles, where they simply

reflect the source function in the outer atmosphere. However, the contribution to the equivalent widths of these Doppler cores is small. More important is the contribution from the line wings, where the line broadening is dominated by the Stark effect and the profile function is very well approximated by (see Unsoeld 1968, p. 323 or Mihalas 1978, p. 296)

$$\Phi(\Delta\nu) \propto n_E \Delta\lambda^{-2.5}. \quad (20)$$

n_E is the local electron density. The continuum absorption coefficient at the wavelength of $H\delta$ is well described by

$$\kappa_V^c = n_E \sigma_E (1 + n_E f(\lambda, T) \sigma / \sigma_E). \quad (21)$$

σ is a cross section of 10^{-18} cm^2 and σ_E is the cross section for Thompson scattering at free electrons. The function $f(\lambda, T)$ contains the contributions of all continuous true absorption processes, but is dominated by hydrogen free-free and bound-free absorption. In LTE a good approximation (better than 10%) in the range between 8000 K and 15000 K and at the wavelength of $H\delta$ is

$$f(\lambda, T) \approx 1.06 \cdot 10^{-19} T_4^{-3} \quad (22)$$

in units of cm^3 . T_4 is the temperature in units of 10^4 K. NLTE effects in the third level of hydrogen can have a small influence on $f(\lambda, T)$, but will change mostly the value of the constant but not the temperature dependence. The occupation number of hydrogen in the second level is given by

$$n_2 \propto b_2 n_E^2 T^{-1.5} \exp(E_2/kT) \quad (23)$$

with b_2 the non-LTE departure coefficient and E_2 the ionization energy from the second level. k is the Boltzmann constant. For this equation we have assumed that most of the free electrons in the atmospheres come from hydrogen, a valid approximation. In our temperature range we find that we can approximate (within 25%)

$$T_4^{-1.5} \exp(E_2/kT) \approx 6.310^1 T_4^{-6} \quad (24)$$

This leads to the following expression for the line strength β_V

$$\beta_v \propto (n_E T_4^{-3})^2 / (1 + 1.06 \cdot 10^{-19} n_E T_4^{-3} \sigma / \sigma_E). \quad (25)$$

Thus, the line strength in the wings of the hydrogen Balmer lines is obviously a function of electron density divided by the third power of temperature in the layers of the formation of line wings, which is close to the continuum optical depth $\tau_v^c = 2/3$. It is straightforward to estimate $n_E T^{-3}$ in these layers. Starting from the hydrostatic equation

$$dP/d\tau_v^c = -g(1 - \Gamma)\rho/\kappa_v^c \quad (26)$$

and with $\rho = m_p n_p (1 + 4Y)$, $n_p = n_E$, $P = n_E (2 + Y) kT$ and ρ , P , n_p , Y being mass density, gas pressure, proton number density and number ratio of helium to hydrogen, respectively, we obtain a differential equation for the electron density as a function of continuum optical depth (making the usual assumption that the logarithmic density gradient is much larger than the logarithmic temperature gradient), which reads

$$(1 + n_E f(\lambda, T) \sigma / \sigma_E) dn_E = A(g, \Gamma, T) d\tau_v^c, \quad (27)$$

where

$$A(g, \Gamma, T) = g(1 - \Gamma) m_p (1 + 4Y) / (\sigma_E (2 + Y) kT) \quad (28)$$

Γ is the usual Eddington-ratio of Thompson scattering radiative acceleration divided by gravity, namely (assuming again $n_E = n_p$)

$$\Gamma = 7.49 T_4^4 (1 + Y) / (g(1 + 4Y)) \propto g_F^{-1} \quad (29)$$

The integration of this differential equation is simple (again regarding the temperature gradient as negligible). We obtain at every continuum optical depth τ_c

$$n_E + n_E^2 \sigma f(\lambda, T) / (2\sigma_E) = A(g, \Gamma, T) \tau_v^c \quad (30)$$

or

$$n_E \sigma f(\lambda, T) / \sigma_E = (1 + 2A(g, \Gamma, T) \tau_v^c \sigma f(\lambda, T) / \sigma_E)^{1/2} - 1. \quad (31)$$

With $f(\lambda, T) \propto T^{-3}$ we see immediately that

$$n_E T^{-3} \propto (1 + g_F(1 - \Gamma) * const.)^{1/2}. \quad (32)$$

which means that the line strength β_V depends solely on the flux weighted gravity and not on effective temperature. We also note that depending on whether the second term under the square root is small or large compared with unity (i.e. $g_F(1 - \Gamma)$ small or large) we will have $n_E T^{-3} \propto g_F(1 - \Gamma)$ or $\propto (g_F(1 - \Gamma))^{0.5}$, respectively. Numerical solutions of the exact problem including full NLTE opacities and the temperature gradient show that this simple estimate is qualitatively correct and fairly accurate.

These simple calculations explain the physical reason why the the strengths of the Balmer lines depend mostly on the flux weighted gravity and why the isocontours of the equivalent widths in Fig. 30 are horizontal. However, they do not explain, why the isocontours bend upwards at higher temperature. The reason is the recombination of hydrogen at lower temperatures. While it is intuitively clear that recombination must lead to stronger hydrogen lines and thus to an upward turn of the isocontours, we verified this by simple numerical calculations solving the same problem as above but including the effects of recombination through the Saha formula. We also included the effects of atmospheric temperature stratifications by allowing for appropriate $T(\tau_V^c)$ relationships. At lower T_{eff} and higher $\log g$ hydrogen partly recombines. κ_V^c becomes smaller ($\propto n_E^2$) and τ_V^c is reached in much larger geometrical depth of much higher pressure and total number density. As a result, the effect of recombination is overcompensated and n_E at the optical depth of line wing formation is much larger than in the calculation without recombination at these temperatures and gravities.

6.2. The FGLR of NGC 300

With 24 A supergiants studied in this work and the 6 early type B supergiants investigated by Urbaneja et al. (2005) we have a large sample, which we can use for an observational test of the FGLR. For the A supergiants, all the data and their uncertainties have been discussed in the previous chapters. A similar discussion has been given by Urbaneja et al. (2005) for the B supergiants. Note, however, that Urbaneja et al. (2005) used the ground-based photometry by Bresolin et al. (2002), which as discussed above has been superseded by the HST/ACS photometry presented and discussed by Bresolin et al. (2005). With the effective temperatures, gravities and intrinsic energy distributions determined for each B supergiant by Urbaneja et al. (2005) we have used the new photometry to re-determine interstellar reddening and extinction, which then yields new stellar radii and absolute V and bolometric magnitudes. Note that Urbaneja et al. (2005) also used the old distance modulus by Freedman et al. (2001), which is significantly different from the new distance modulus determined by Gieren et al. (2005a) based on on optical and IR observations of a large

sample of Cepheids minimizing the errors caused by reddening.

The result is shown in Fig. 31, which reveals a clear and rather tight relationship of flux weighted gravity $\log g_F$ with bolometric magnitude M_{bol} . A simple linear regression yields $b_{FGLR} = 8.11$ for the zero point and $a_{FGLR} = -3.52$ for the slope. The standard deviation from this relationship is $\sigma = 0.34$ mag.

We also overplot the FGLRs predicted by stellar evolution theory (Meynet & Maeder 2005) as discussed in the previous paragraphs. At lower luminosities (or large $\log g_F$) they agree well with the observed linear regression. In particular, the FGLR for Milky Way metallicity is very close. For higher luminosities (or small $\log g_F$) the linear regression and the stellar evolution FGLRs diverge because of the curvature of the latter, which is caused by the fact that the exponent of the mass-luminosity relationship becomes smaller. Looking at the scatter of the data points around either the linear regression or the FGLR for Milky Way metallicity it is hard to tell which of the two is the better fit. Approximating the stellar evolution FGLRs by

$$\begin{aligned} M_{bol} &= \alpha(\log g_F)(\log g_F - x_0) + M_{bol}^0 \\ \alpha(\log g_F) &= \alpha_0 + \alpha_1(x_0 - \log g_F) + \alpha_2(x_0 - \log g_F)^2 \end{aligned} \quad (33)$$

(values for $\alpha_0, \alpha_1, \alpha_2$ and x_0 are given in Table 4) we can calculate standard deviations to characterize the scatter around those. For Milky Way metallicity we obtain $\sigma = 0.35$ mag, practically identical to scatter around the linear regression. The FGLR for SMC metallicity has a much stronger curvature (as the result of less mass-loss in the O-star stage of stellar evolution) and is shifted towards higher luminosities and seems to be worse fit of the data. This is confirmed by the standard deviation of $\sigma = 0.41$ mag for this relationship. Applying a vertical shift of $\Delta M_{bol}^0 = 0.16$ mag to the SMC metallicity relationship minimizes its standard deviation to $\sigma = 0.38$ mag, still worse than for the linear regression and the FGLR for Milky Way metallicity. We note that most of our objects have metallicities between the Milky Way and the SMC comparable to the LMC. Unfortunately, no complete set of models including the effects of rotation in the mass range needed is available at this metallicity at the moment.

The new linear regression coefficients for the FGLR in NGC 300 are different from those obtained by Kudritzki, Bresolin & Przybilla (2003) ($a_{FGLR} = -3.85$ and $b_{FGLR} = 7.96$) resulting now in a higher luminosity zero point and a somewhat shallower slope. This is caused by a combination of different factors, a new distance modulus to NGC 300, improved HST photometry leading to larger extinction and a systematic change of stellar parameters as the result of the new diagnostic technique of the low resolution spectra.

6.3. The FGLR averaged over eight galaxies

In their first investigation of the empirical FGLR Kudritzki, Bresolin & Przybilla (2003) have added A supergiants from six Local Group galaxies with stellar parameters obtained from quantitative studies of high resolution spectra (Milky Way, LMC, SMC, M31, M33, NGC 6822) to their results for NGC 300 to obtain a larger sample. They also added 4 objects from the spiral galaxy NGC 3621 (at 6.7 Mpc) which were studied at low resolution. We will add exactly the same data set to our new enlarged NGC 300 sample, however, with a few minor modifications. For the Milky Way we include the latest results from Przybilla et al. (2006) and Schiller & Przybilla (2007) and for the two objects in M31 we use the new stellar parameters obtained by Przybilla et al. (2008). For the objects in NGC 3621 we apply new HST photometry. (Note that for the objects T_{eff} and $\log g$ were obtained from a spectral fit assuming LMC metallicity, i.e. the detailed technique developed here for the NGC 300 objects has not yet been applied. However, eliminating those objects from the sample does not change the results significantly). We have also re-analyzed the LMC objects using ionization equilibria for the temperature determination. The results are summarized in Table 5. The bolometric corrections for all objects are calculated using eq.(6).

Fig. 32 shows bolometric magnitudes and flux-weighted gravities for this full sample of eight galaxies revealing a tight relationship over one order of magnitude in flux-weighted gravity. The linear regression coefficients are $a_{FGLR} = -3.41 \pm 0.16$ and $b_{FGLR} = 8.02 \pm 0.04$, very similar to the NGC 300 sample alone. The standard deviation is $\sigma = 0.32$ mag. The new coefficients are slightly different from the previous work by Kudritzki, Bresolin & Przybilla (2003) ($a_{FGLR} = -3.71$ and $b_{FGLR} = 7.92$) resulting in a FGLR brighter by 0.1 to 0.2 mag now in much closer agreement with stellar evolution. Compared with the new results the stellar evolution FGLR for Milky Way metallicity provides a fit of almost similar quality with a standard deviation of $\sigma = 0.31$ mag. The stellar evolution FGLR fit for SMC metallicity is worse with $\sigma = 0.42$ mag (applying $\Delta M_{bol}^0 = 0.20$ mag reduces the standard deviation to $\sigma = 0.35$ mag).

We conclude that the simple linear regression fit of this sample is the best way to describe the empirical FGLR at this point. It is basically in agreement with stellar evolution theory, at least if mass-loss and rotational mixing affect the evolution as for the models with solar metallicity. We note that for the evolutionary models accounting for mass-loss and mixing based on SMC metallicity we have an offset relative to the observed FGLR by about 0.20 mag and a curvature stronger than observed. Again, we stress the need for a complete set of models including the effects of rotation at LMC metallicities.

7. Conclusions and Future Work

The goal of this work has been to demonstrate the astrophysical potential of low resolution spectroscopy of A supergiant stars in galaxies beyond the Local Group. By introducing a novel method for the quantitative spectral analysis we are able to determine accurate stellar parameters, which allow us to test stellar evolution models including the evolutionary time scales in the A supergiant stage. Through the spectroscopic determination of stellar parameters we can also constrain interstellar reddening and extinction by comparing the calculated SED with broad band photometry. We find a very patchy extinction pattern as to be expected for a star forming spiral galaxy. The average extinction is in agreement with multi-wavelength studies of Cepheids including K-band photometry.

The method also allows to determine stellar metallicities and to study stellar metallicity gradients. We find a metallicity close to solar in the center of NGC 300 and a gradient of -0.08 dex/kpc. To our knowledge this is the first systematic stellar metallicity study in galaxies beyond the Local Group focussing on iron group elements. In the future the method can be extended to not only determine metallicity but also the ratio of α - to iron group elements as a function of galactocentric distance. The stellar metallicities obtained can be compared with oxygen abundance studies of HII regions using the strong line method. This allows us to discuss the various calibrations of the strong line method, which usually yield very different results.

The improved spectral diagnostic method presented here enables us to very accurately determine stellar flux weighted gravities $\log g_F = \log g/T_{\text{eff}}^4$ and bolometric magnitudes, which we explain by a detailed discussion of the physical background of the spectroscopic diagnostics. We find that above a certain threshold in effective temperature a simple measurement of the strengths of the Balmer lines can be used to determine accurate values of $\log g_F$.

Absolute bolometric magnitudes M_{bol} and flux-weighted gravities $\log g_F$ are tightly correlated. It is shown that such a correlation is expected for stars, which evolve at constant luminosity and mass. We discuss the observed “flux-weighted gravity - luminosity relationship (FGLR)” in detail and compare with stellar evolution theory. We find reasonable agreement with evolutionary tracks which account for mass-loss and rotational mixing assuming solar metallicity. The agreement is less good for similar tracks with SMC metallicity.

With a relatively small residual scatter of $\sigma = 0.3$ mag the observed FGLR is an excellent tool to determine accurate spectroscopic distance to galaxies. It requires multicolor photometry and low resolution (5\AA) spectroscopy to determine effective temperature and gravity and, thus, flux-weighted gravity directly from the spectrum using the self-consistent method developed here. With effective temperature, gravity and metallicity determined we also know the bolometric correction, which is small for A supergiants, which means that errors in the stellar parameters do not largely

affect the determination of bolometric magnitudes. Moreover, we know the intrinsic stellar SED and, therefore, can determine interstellar reddening and extinction from the multicolor photometry, which will allow the accurate determination of the reddening-free apparent bolometric magnitude. The application of the FGLR will then yield absolute magnitudes and, thus, the distance modulus. With the intrinsic scatter of $\sigma = 0.3$ mag and 30 targets per galaxy one can estimate an accuracy of 0.05 mag in distance modulus (0.1 mag for 10 target stars).

The advantage of the FGLR method for distance determinations is its spectroscopic nature, which provides significantly more information about the physical status of the objects used for the distance determination than simple photometry methods. Most importantly, metallicity and interstellar extinction can be determined directly. The latter is crucial for spiral and irregular galaxies because of the intrinsic patchiness of reddening and extinction.

Since supergiant stars are known to show intrinsic photometric variability, the question arises whether the FGLR method is affected by such variability. For the our targets in NGC 300 this issue has been carefully investigated by Bresolin et al. (2004), who studied their CCD photometry lightcurves obtained over many epochs in the parallel search for Cepheids in NGC 300. They concluded that amplitudes of photometric variability are very small and do not affect distance determinations using the FGLR method. The standard deviations from the mean V magnitude for subset of A supergiants identified as variable ranges between 0.03 to 0.05 magnitudes, with maximum amplitudes of the variability between 0.08 to 0.23 mag. This is clearly within the one σ uncertainty found for the FGLR.

The effects of crowding and stellar multiplicity are also important. However, in this regard A supergiants offer tremendous advantages relative to other stellar distance indicators. First of all, they are significantly brighter. Bresolin et al. (2005) using HST ACS photometry compared to ground-based photometry have studied the effects of crowding on the Cepheid distance to NGC 300 and concluded that they are negligible. With A supergiants being 3 to 6 magnitudes brighter than Cepheids it is clear that even with ground-based photometry only crowding is generally not an issue for these objects at the distance of NGC 300 and, of course, with HST photometry (and in the future JWST) one can reach much larger distances before crowding becomes important. In addition, any significant contribution by additional objects to the light of an A supergiant will become apparent in the spectrum, if the contaminants are not of a very similar spectral type, which is very unlikely because of the short evolutionary lifetime in the A supergiant stage. It is also important to note that A supergiants have evolutionary ages larger than 10 million years, which means that they have time to migrate into the field or that they are found in older clusters, which are usually less concentrated than the very young OB associations.

It is evident that the type of work described in this paper can be in a straightforward way extended to the many spiral galaxies in the local volume at distances in the 4 to 7 Mpc range.

Pushing the method we estimate that with present day 8m to 10m class telescopes and the existing very efficient multi-object spectrographs one can reach down with sufficient S/N to $V = 22.5$ mag in two nights of observing time under very good conditions. For objects brighter than $M_V = -8$ mag this means metallicities and distances can be determined out to distances of 12 Mpc ($m-M = 30.5$ mag). This opens up a substantial volume of the local universe for metallicity and galactic evolution studies and independent distance determinations complementary to the existing methods. With the next generation of extremely large telescopes such as the TMT, GMT or the E-ELT the limiting magnitude can be pushed to $V = 24.5$ equivalent to distances of 30 Mpc ($m-M = 32.5$ mag).

Acknowledgements: WG and GP gratefully acknowledge financial support from the Chilean FONDAPE Center of Astrophysics under grant 15010003, and from the Chilean Centro de Astrofísica y Tecnologías Afines (CATA). We like to thank Vivan U and John Hillier for the careful reading of the manuscript and stimulating discussion. We also thank the anonymous referee for his constructive suggestions, which helped to improve the paper.

REFERENCES

- Allende Prieto, C., Lambert, D.L., & Asplund, M. 2001, *ApJ*, 556, L63
- Aufdenberg, J. P., Hauschildt, P.H., Baron, E. et al. 2002, *ApJ*, 570, 344
- Aydin, C., 1972, *A&A*, 19, 369
- Bonanos, C., Stanek, K., Kudritzki, R.P. et al. 2006, *ApJ*, 652, 313
- Bresolin, F., Kennicutt, R. et al. 1996, *AJ*, 112, 1009
- Bresolin, F., Kennicutt, R. et al. 1998, *AJ*, 116, 119
- Bresolin, F., Kudritzki, R.-P., Méndez, R. H., & Przybilla, N. 2001, *ApJ*, 548, L159
- Bresolin, F., Gieren, W., Kudritzki, R.-P., Pietrzyński, G., & Przybilla, N. 2002, *ApJ*, 567, 277
- Bresolin, F., Pietrzyński, G., Gieren, W., Kudritzki, R.-P., Przybilla, N. & Fouque, P. 2004, *ApJ*, 600, 182
- Bresolin, F., Pietrzyński, G., Gieren, W. & Kudritzki, R. P. 2005, *ApJ*, 634, 1020
- Buser, R. & Kurucz, R.L. 1978, *A&A*, 70, 555
- Cardelli, J. A., Clayton, G. C. & Mathis, J. S. 1989, *ApJ*, 345, 245

- Deharveng, L., Caplan, J., Lequeux, J., Azzopardi, M., Breysacher, J., Tarengi, M., Westerlund, B. 1988, A&AS, 73, 407
- Denicolo, G., Terlevich, R. & Terlevich, E. 2002, MNRAS, 330, 69
- Dopita, M.A., Evans, I.N. 1986, ApJ, 307, 431
- Evans, C. J. & Howarth, I.D. 2003, MNRAS, 345, 1223
- Freedman et al. 2001, ApJ, 553, 47
- Grevesse, N. & Sauval, A. J. 1998, Space Science Reviews, 85, 161
- Gieren, W., Pietrzyński, G., Soszynski, I., Bresolin, F., Kudritzki, R. P., Miniti, D., & Storm, J. 2005, ApJ, 628, 695
- Gieren, W. et al. 2005, ESO Messenger, 121, 23
- Gieren, W., Pietrzyński, G., Nalewajko, K. et al. 2006, ApJ, 647, 1056
- Groth, H. G. 1961, ZAp, 51, 231
- Holland, S. 1998, AJ, 115, 1916
- Kaufer, A., Venn, K. A., Tolstoy, E., Pinte, C. & Kudritzki, R. P. 2004, AJ, 127, 2723
- Kobulnicky, H.A., Kennicutt, R.C. & Pizagno, J.L. 1999, ApJ, 514, 544
- Kudritzki, R. P. 1973, A&A, 28, 103
- Kudritzki, R.-P., Lennon, D. J. & Puls, J. 1995, *Quantitative spectroscopy of luminous blue stars in distant galaxies*, in Proc. ESO Workshop "Science with VLT", Eds. J. P. Welsh & I. J. Danziger
- Kudritzki, R.P., 1998, *Quantitative spectroscopy of the brightest blue supergiant stars in galaxies*, in "Stellar Physics for the Local Group", eds. A. Aparicio, A. Herrero & F. Sanchez (Cambridge University Press), p. 149
- Kudritzki, R.-P., Puls, J., Lennon, D. J. et al. 1999, A&A, 350, 970
- Kudritzki, R.-P., Bresolin, F., & Przybilla, N. 2003, ApJ, 582, L83
- McCarthy, J. K., Lennon, D. J., Venn, K. A., Kudritzki, R. P., Puls, J. & Najarro, F. 1995, ApJ, 455, L135

- McCarthy, J. K., Kudritzki, R. P., Lennon, D. J., Venn, K.A. & Puls, J. 1997, *ApJ*, 482, 757
- Meynet, & Maeder, A. 2005, *A&A*, 429, 581
- Mihalas, D. 1978, *Stellar Atmospheres*, W.H. Freeman and Company, 2nd edition
- Pettini, M. & Pagel, B.E.J. 2004, *MNRAS*, 348, L59
- Pilyugin, L.S. 2001, *A&A*, 369, 594
- Przybilla, N., Butler, K., Becker, S. R., Kudritzki, R. P. & Venn, K.A. 2000, *A&A*, 359, 1085
- Przybilla, N., Butler, K., Becker, S. R., & Kudritzki, R. P. 2001a, *A&A*, 369, 1009
- Przybilla, N., Butler, K. & Kudritzki, R. P. 2001b, *A&A*, 379, 936
- Przybilla, N. & Butler, K. 2001, *A&A*, 379, 955
- Przybilla, N. 2002, thesis, Fakultät fuer Physik, Ludwig-Maximilian University, Munich
- Przybilla, N., Butler, K., Becker, S. R., & Kudritzki, R. P. 2006a, *A&A*, 445, 1099
- Przybilla, N., Butler, K., & Kudritzki, R. P. 2008, in “The Metal-Rich Universe”, eds. G. Israelian & G. Meynet (Cambridge University Press), in press (astro-ph/0611044)
- Repolust, T., Puls, J., & Herrero, A. 2004, *A&A*, 415, 349
- Schiller, F. & Przybilla, N. 2007, *Astronomische Nachrichten* 328, 656
- Unsoeld, A. 1968, *Physik der Sternatmosphären*, Springer-Verlag, 2. Auflage
- Urbaneja, M. A., Herrero, A. J., Bresolin, F., Kudritzki, R. P., Gieren, W., Puls, J., J. K., Przybilla, N., Najarro, F. & Pietrzynski, G. 2005, *ApJ*, 622, 877
- Venn, K. A. 1995a, *ApJS*, 99, 659
- Venn, K. A. 1995a, *ApJ*, 449, 839
- Venn, K. A. 1999, *ApJ*, 518, 405
- Venn, K. A., McCarthy, J. K., Lennon, D. J., Przybilla, N., Kudritzki, R. P. & Lemke, M. 2000, *ApJ*, 541, 610
- Venn, K. A., Lennon, D. J., Kaufer, A., McCarthy, J. K., Przybilla, N., Kudritzki, R. P., Lemke, M., Skillman, E. D. & Smartt, S. J. 2001, *ApJ*, 547, 765

Venn, K. A., Tolstoy, E. Kaufer, A. et al. 2003, AJ, 126, 1326

Wolf, B.1971, A&A, 10, 383

Wolf, B.1972, A&A, 20, 275

Wolf, B.1973, A&A, 28, 335

Zaritski, D., Kennicutt, R. C. & Huchra, J.P. 1994, ApJ, 420, 87

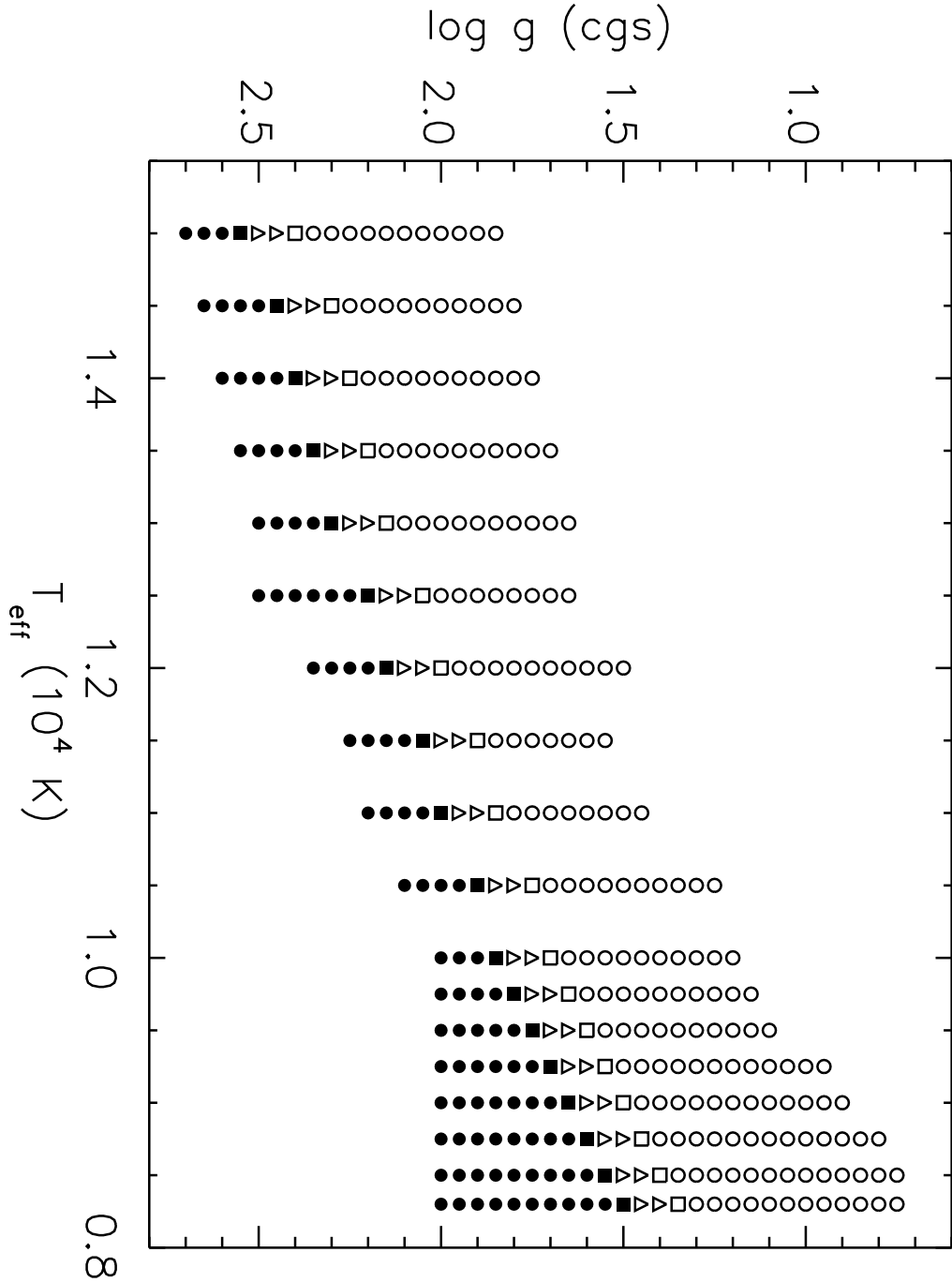


Fig. 1.— Parameter space of the model atmosphere grid used in this study. Different symbols refer to the microturbulence values used for the models. Open circles: $v_t = 8$ km/s; open squares 7 km/sec; open triangles 6 km/sec; filled squares 5 km/sec; filled circles 4 km/sec. At each grid point metallicities from between $[Z] = 0.3$ to -1.30 are available (see text).

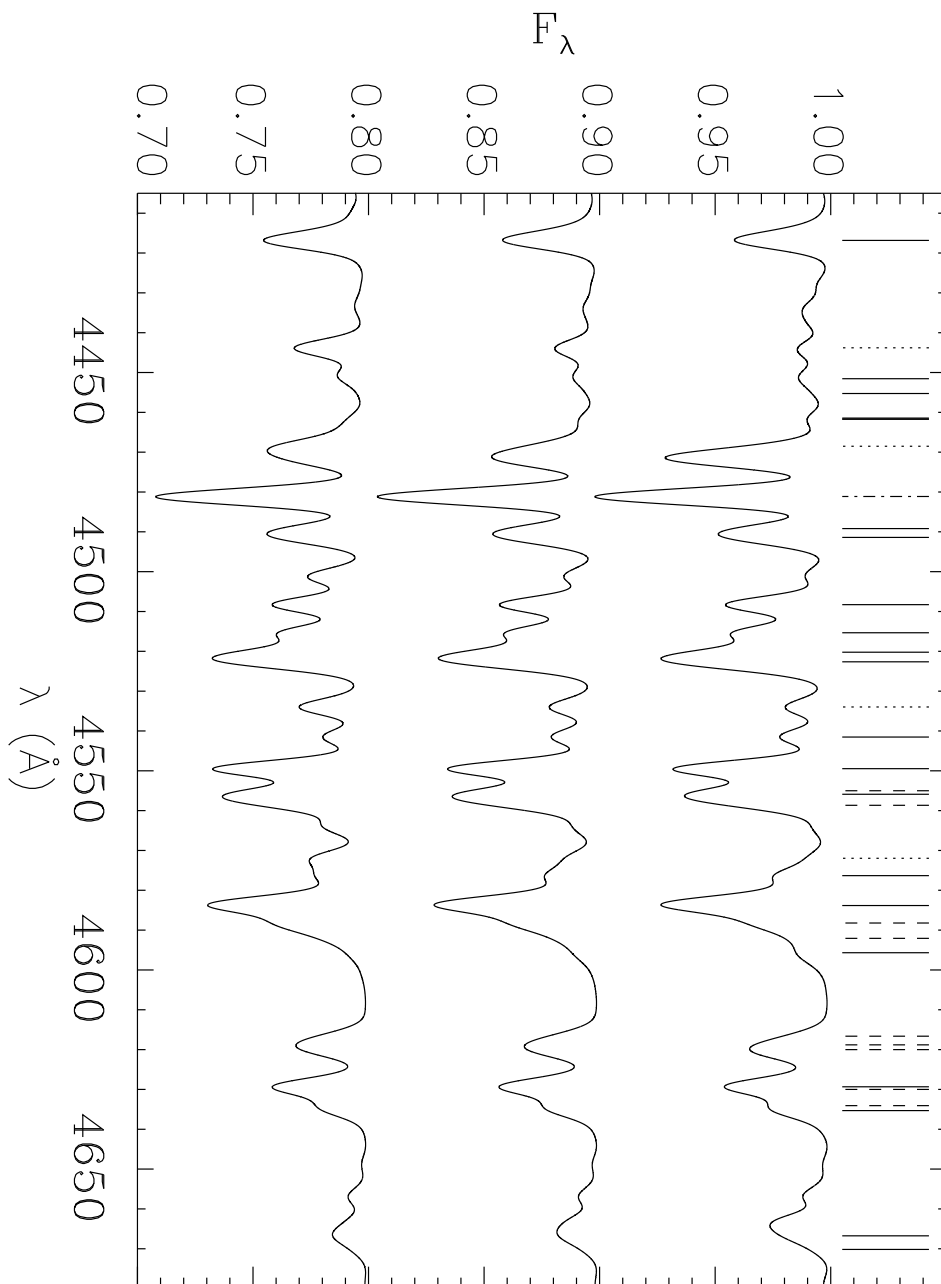


Fig. 2.— The temperature-metallicity degeneracy of spectral types. Synthetic spectra of three A supergiant model atmospheres degraded to 5 \AA resolution with $(T_{\text{eff}}, \log g, [Z]) = (10500 \text{ K}, 1.40, 0.15)$ (top); $(9500 \text{ K}, 1.20, -0.30)$ (middle); $(8750 \text{ K}, 1.00, -0.50)$ (bottom). The latter two are vertically shifted by 0.1 and 0.2. Metal line identifications are given by the bars at the top (solid: FeII; dashed: CrII; dotted: TiII; dashed-dotted: MgII). Note the change of the strength of the HeI line at 4471 \AA from the hottest to the cooler models.

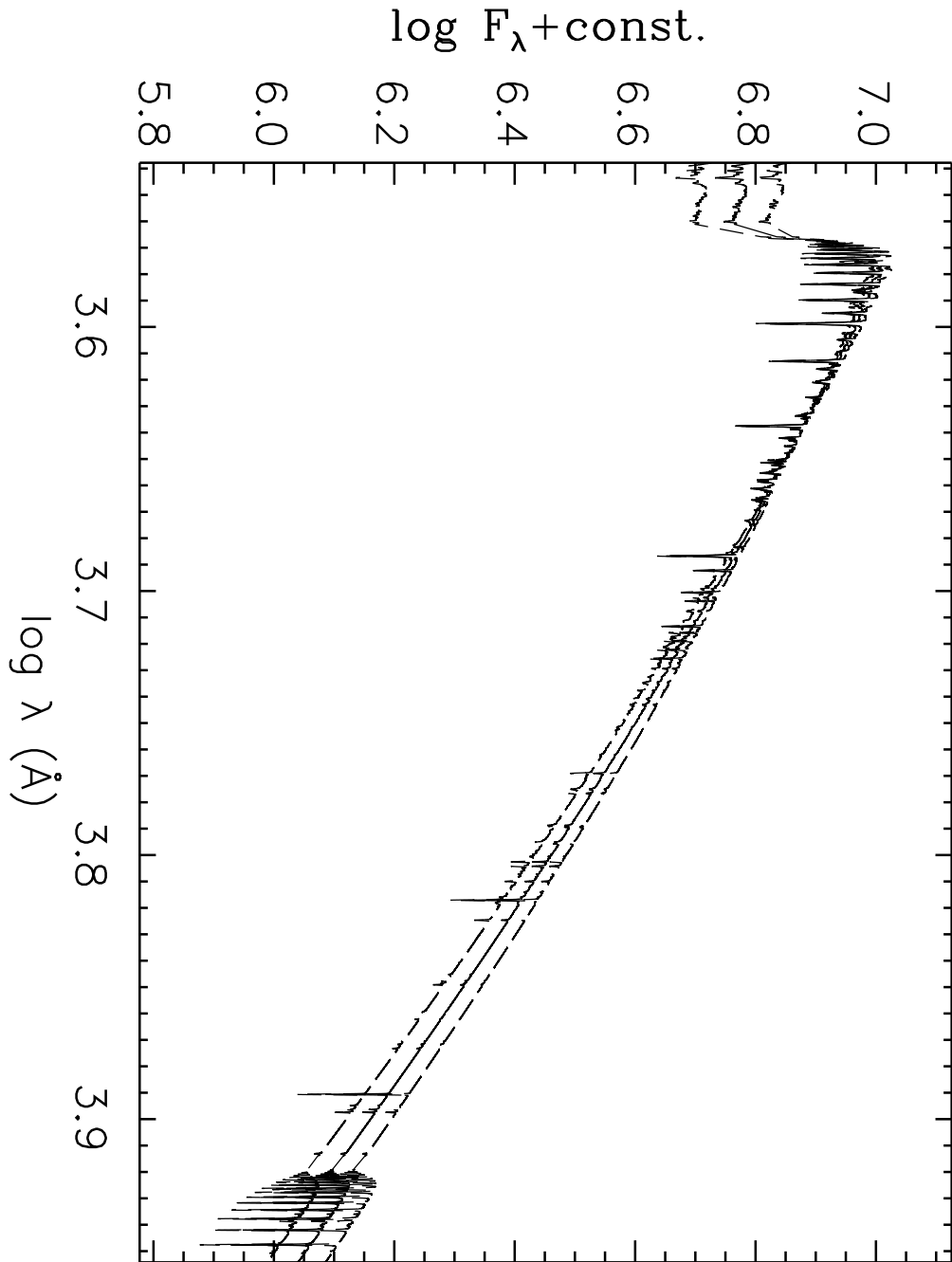


Fig. 3.— Energy distributions of the models of Fig. 2. The fluxes are normalized at 4380 Å. The hottest model has the steepest SED.

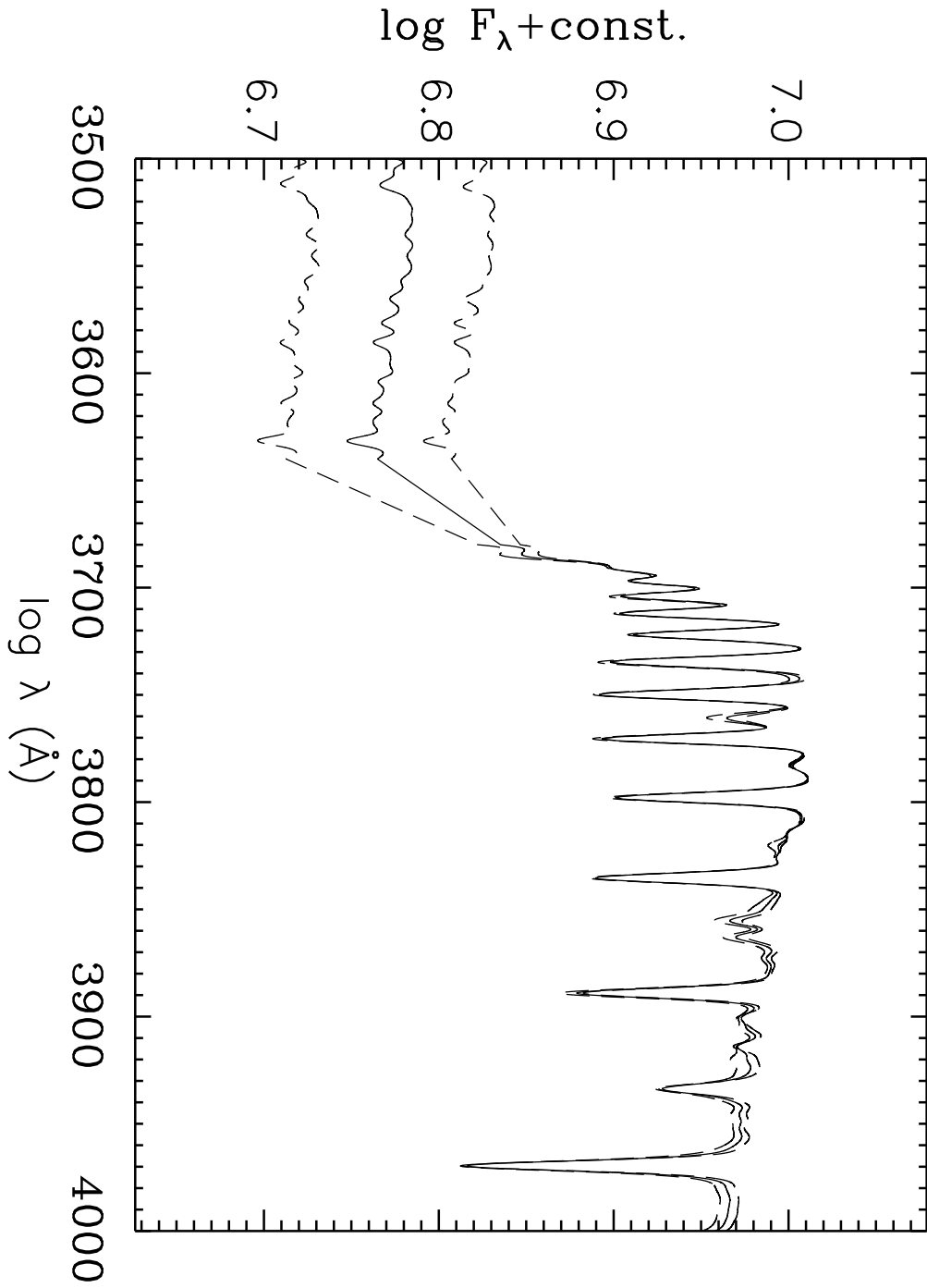


Fig. 4.— Balmer jump fluxes of the models of Fig. 2. The fluxes are normalized at 3790 Å. The hottest model has the smallest Balmer jump.

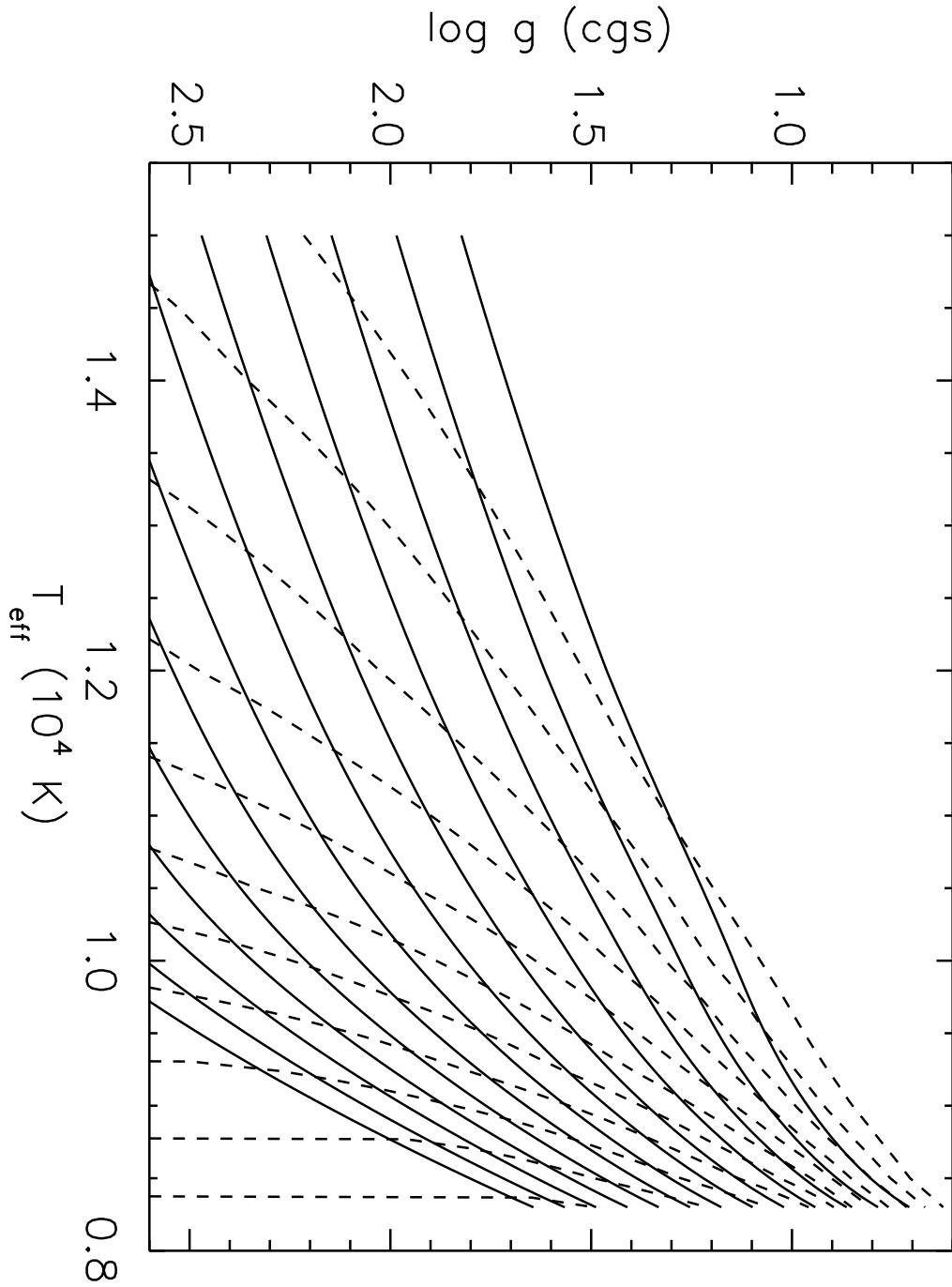


Fig. 5.— Isocontours of $H\delta$ (solid) and D_B (dashed) in the $(\log g, \log T_{\text{eff}})$ plane. $H\delta$ isocontours start with 1 Å equivalent width and increase in steps of 0.5 Å. D_B isocontours start with 0.1 dex and increase by 0.1 dex. The isocontours are calculated from the model atmosphere and non-LTE line formation grid described in section 3 and Fig. 1.

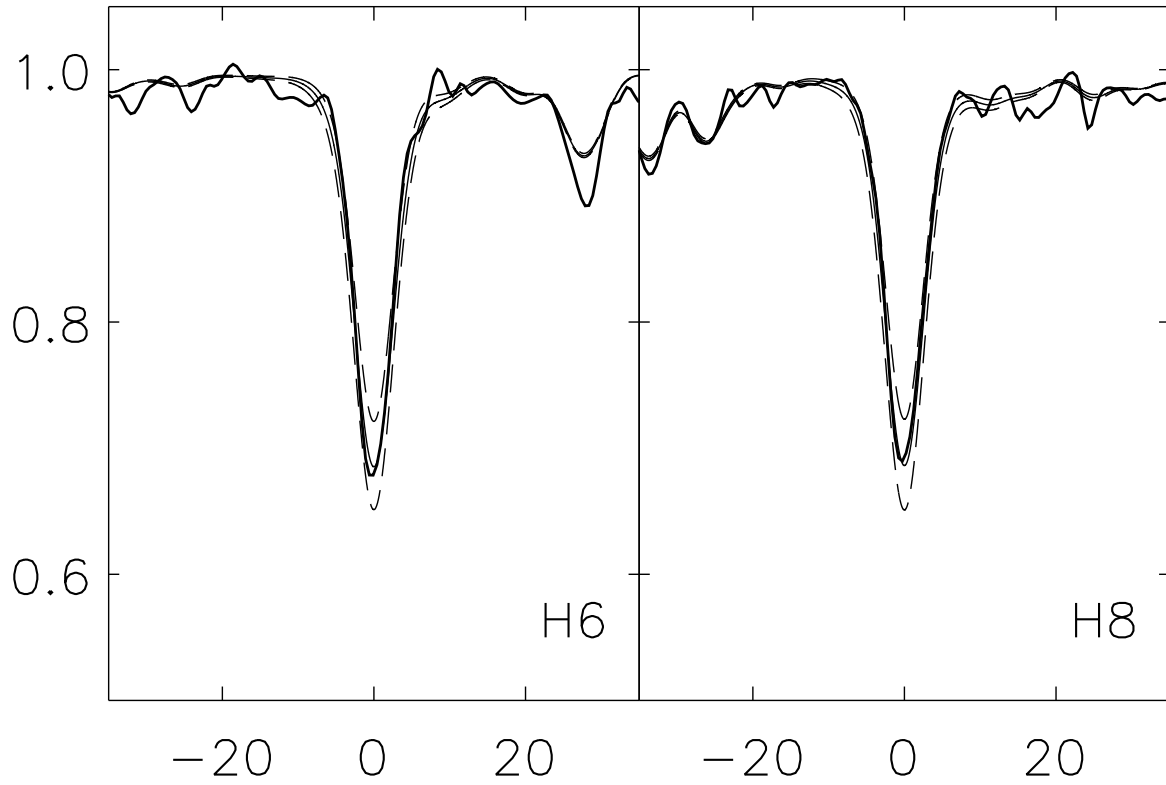


Fig. 6.— Model atmosphere fit of two observed Balmer lines of target No. 21 of Table 1 for $T_{eff} = 10000$ K and $\log g = 1.55$ (solid). Two additional models with same T_{eff} but $\log g = 1.45$ and 1.65 , respectively, are also shown (dashed). Fits of other Balmer lines such as $H_{7,8,9,10}$ are similar. Note that the calculated line profiles were folded with a Gaussian of 5 \AA FWHM to account for instrumental broadening

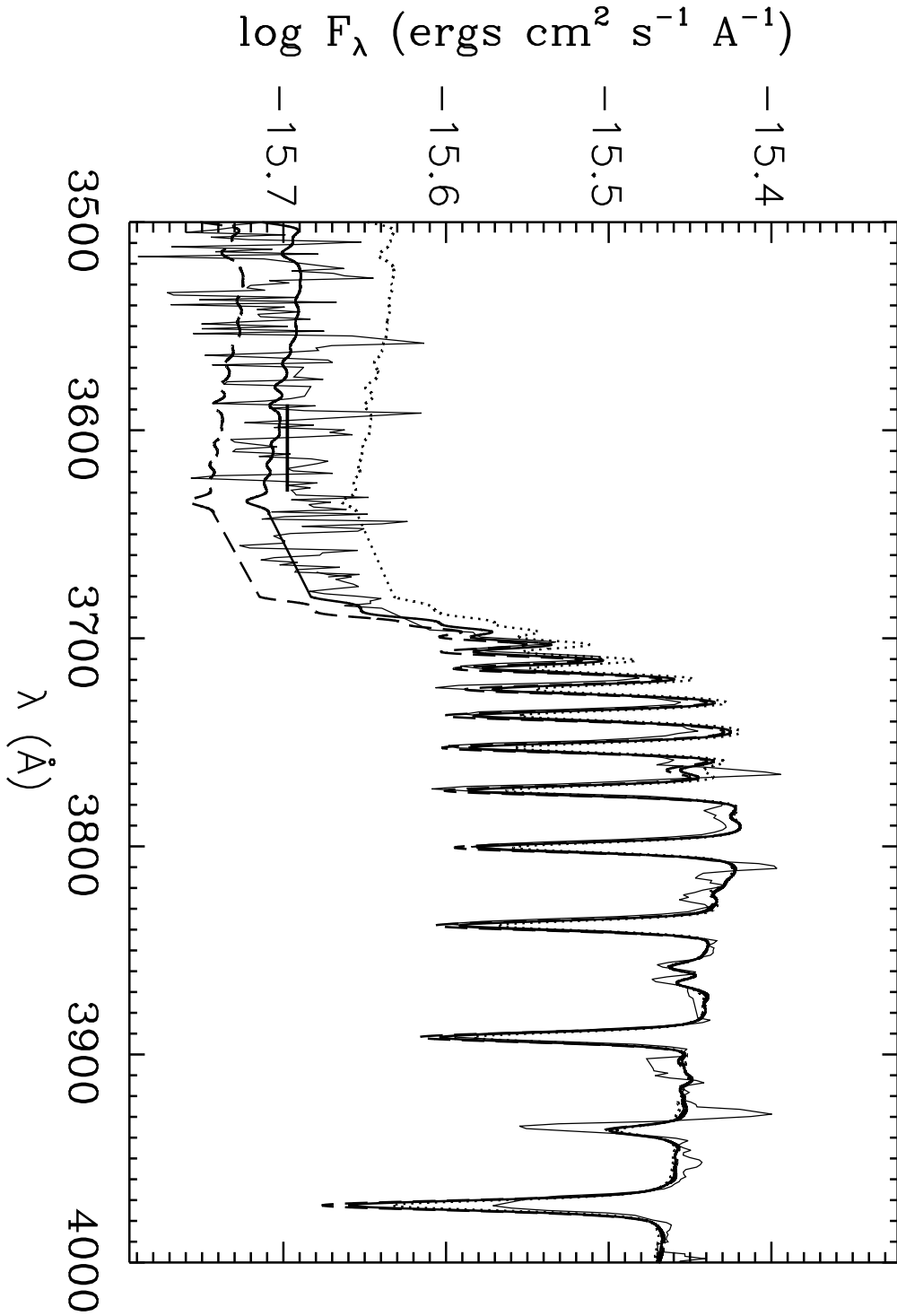


Fig. 7.— Model atmosphere fit of the observed Balmer jump of target No. 21 of Table 1 for $T_{\text{eff}} = 10000$ K and $\log g = 1.55$ (solid). Two additional models with the same $\log g$ but $T_{\text{eff}} = 9750$ K (dashed) and 10500 K (dotted) are also shown. The horizontal bar at 3600 \AA represents the average of the flux logarithm over this wavelength interval, which is used to measure D_B (see text).

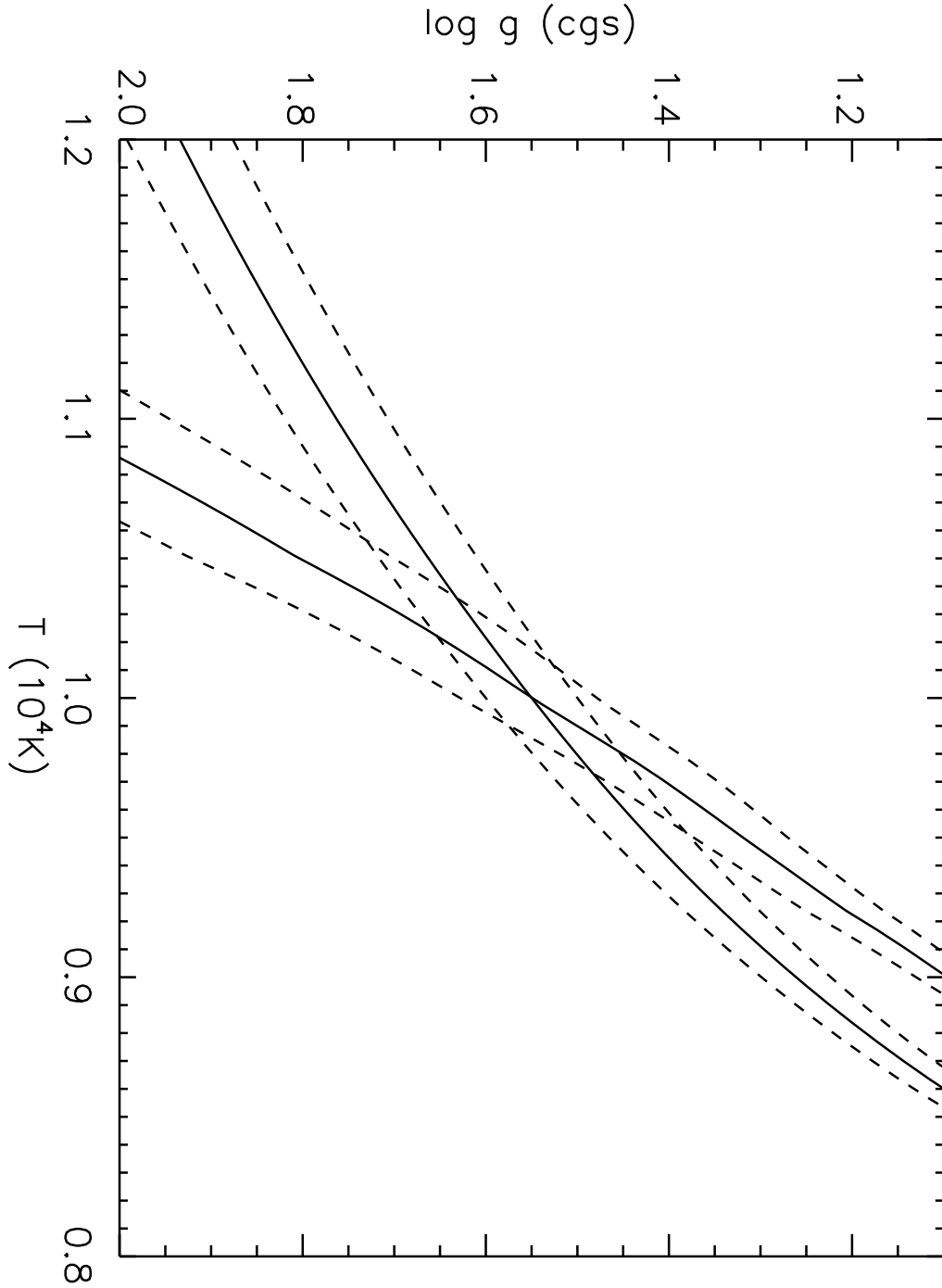


Fig. 8.— $(\log g, \log T_{eff})$ -fit diagram for target No.21 of Table 1. The solid curves represent the best fits of the Balmer jump and the Balmer lines. The dashed curves correspond to the maximum fitting errors.

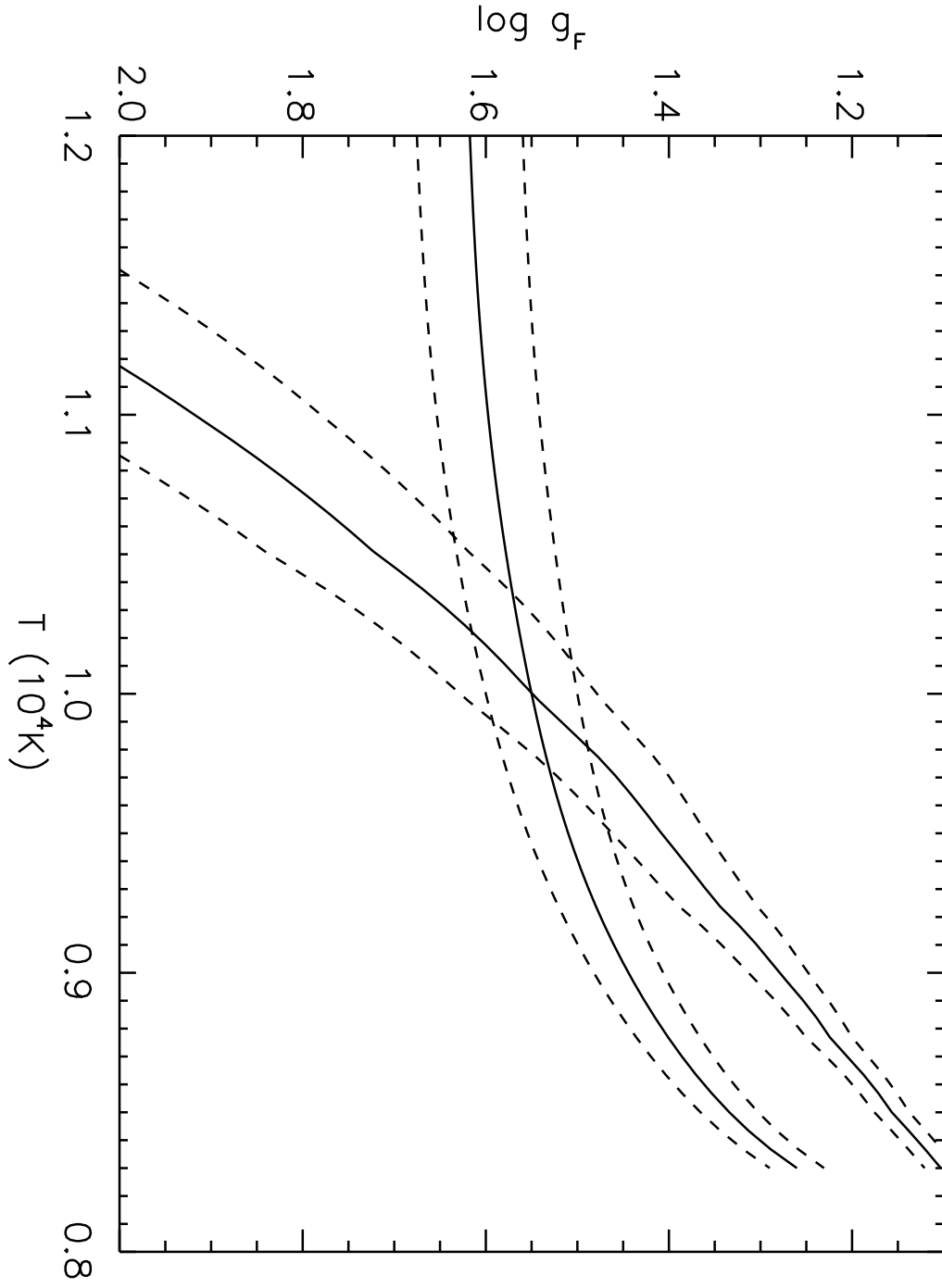


Fig. 9.— Same as Fig. 8 but for the flux weighted gravity $\log g_F$ instead of gravity $\log g$.

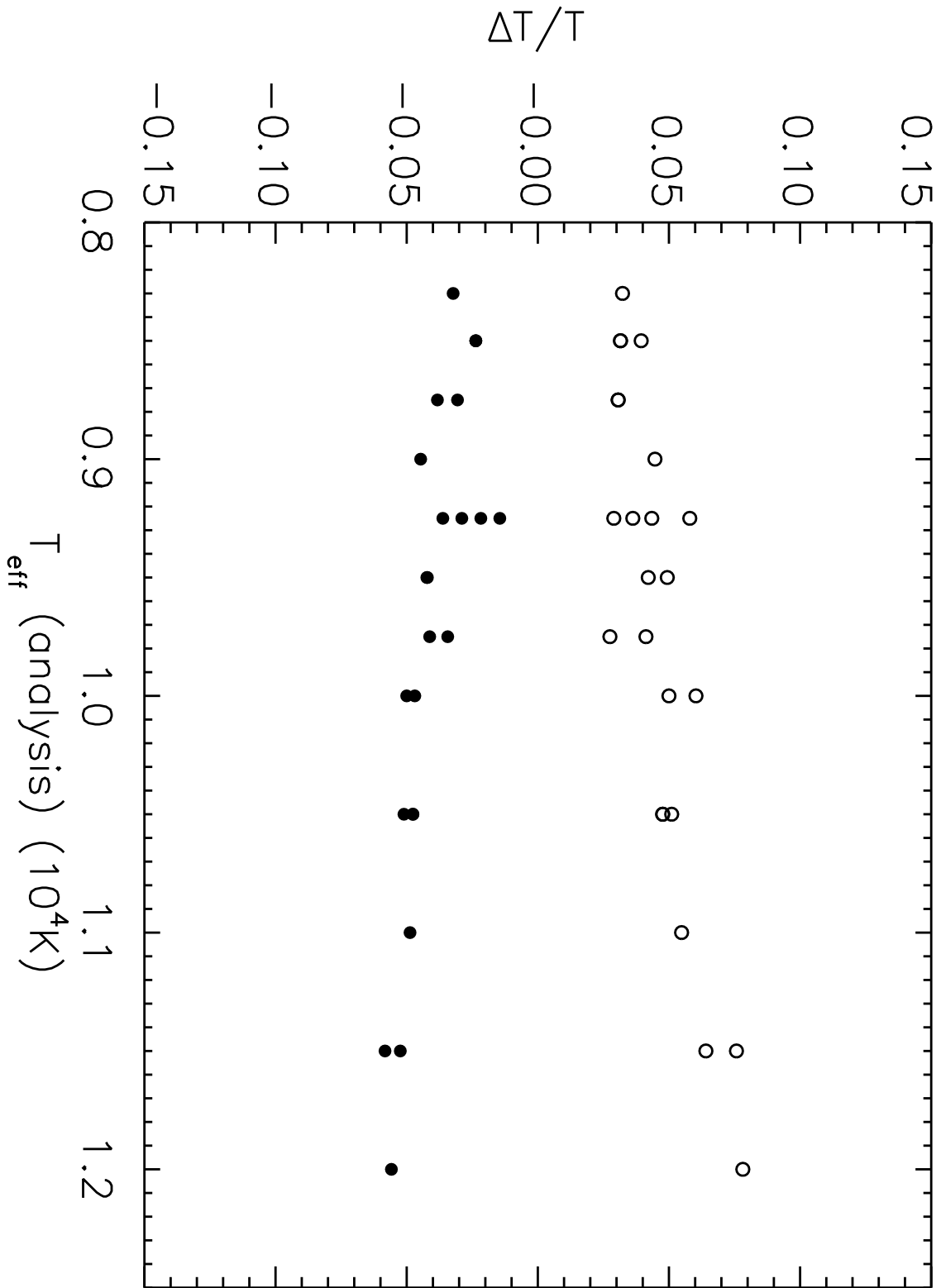


Fig. 10.— Effective temperature uncertainties $\pm\Delta T_{\text{eff}}/T_{\text{eff}}$ as a function of effective temperatures (see Table 1). Open and solid symbols refer to positive and negative errors, respectively.

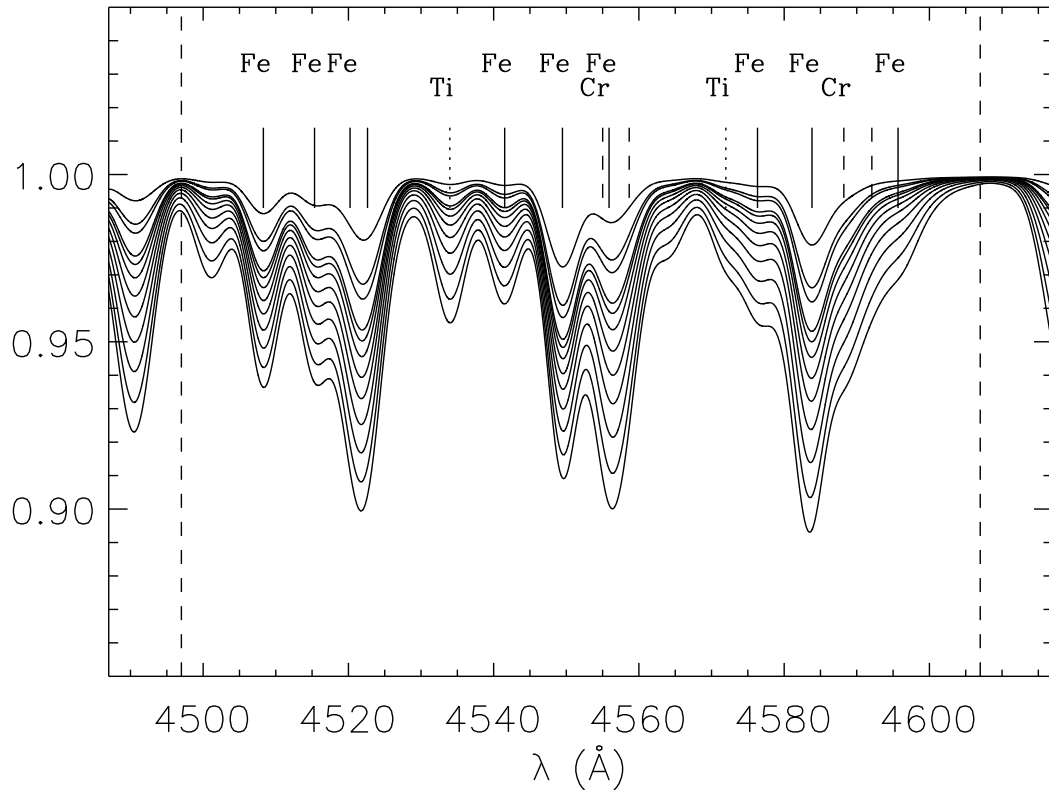


Fig. 11.— Synthetic metal line spectra calculated for the stellar parameters of target No.21 as a function of metallicity in the spectral window from 4497 \AA to 4607 \AA . Metallicities range from $[Z] = -1.30$ to 0.30, as described in the text. The dashed vertical lines give the edges of the spectral window as used for a determination of metallicity. The synthetic spectra were folded with a Gaussian of 5 \AA FWHM to account for the instrumental broadening. Rotational broadening is negligible for A supergiants at this resolution and not taken into account.

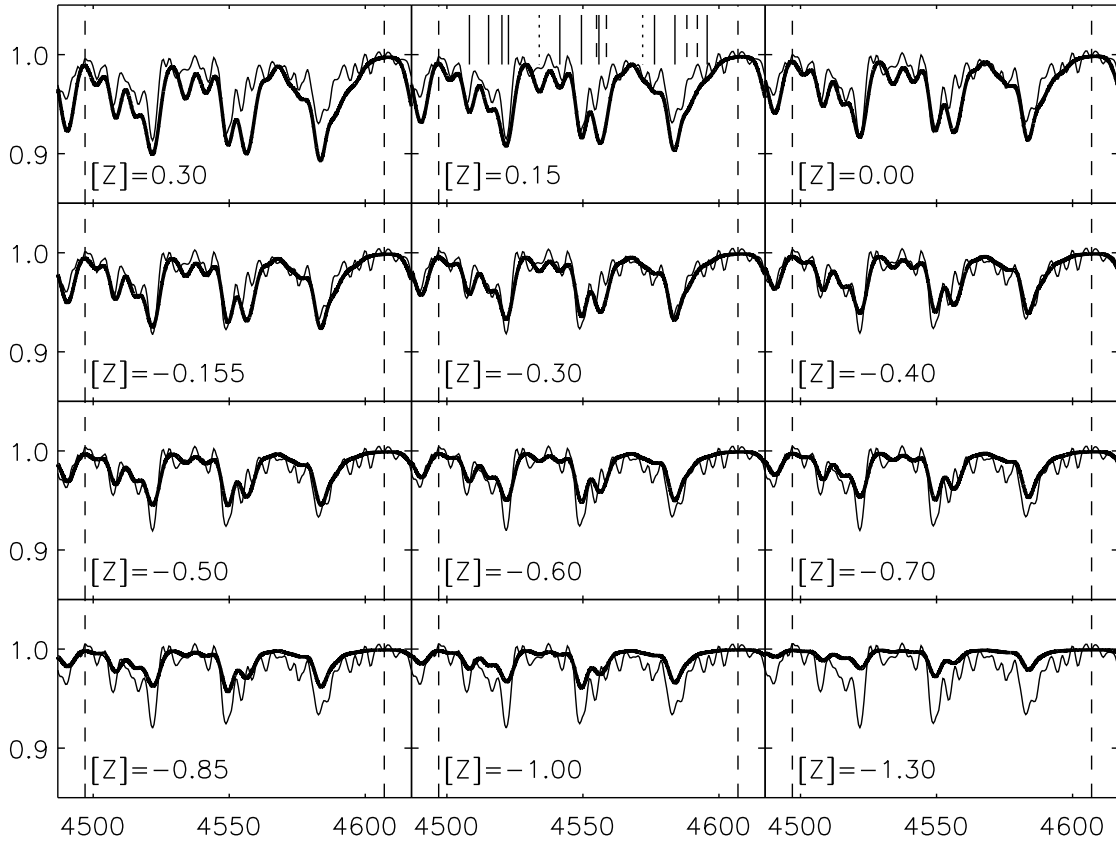


Fig. 12.— Observed spectrum of target No. 21 for the same spectral window as Fig. 11 overplotted by the same synthetic spectra for each metallicity separately. The line identification symbols plotted for $[Z] = 0.15$ are the same as in Fig. 11. For the renormalization of the observed spectrum at each different metallicity see discussion in the text. The abscissae are wavelengths in \AA .

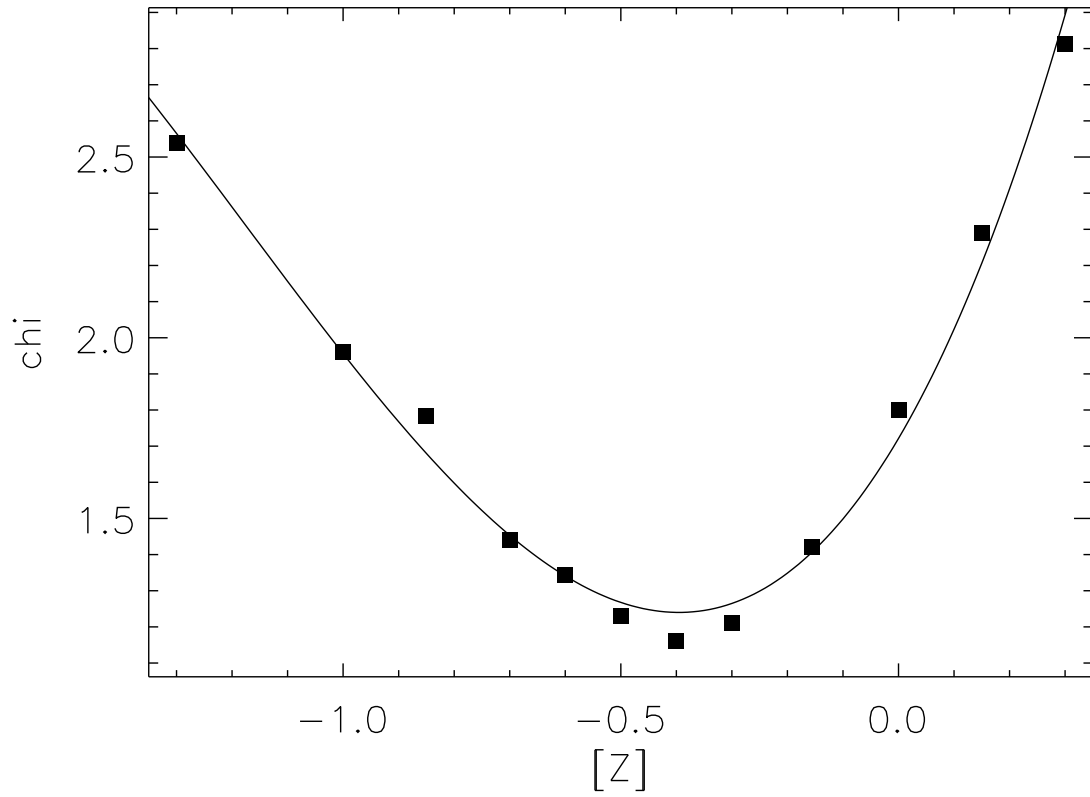


Fig. 13.— $\chi([Z])_i$ as obtained from the comparison of observed and calculated spectra in Fig. 12. The solid curve is a third order polynomial fit.

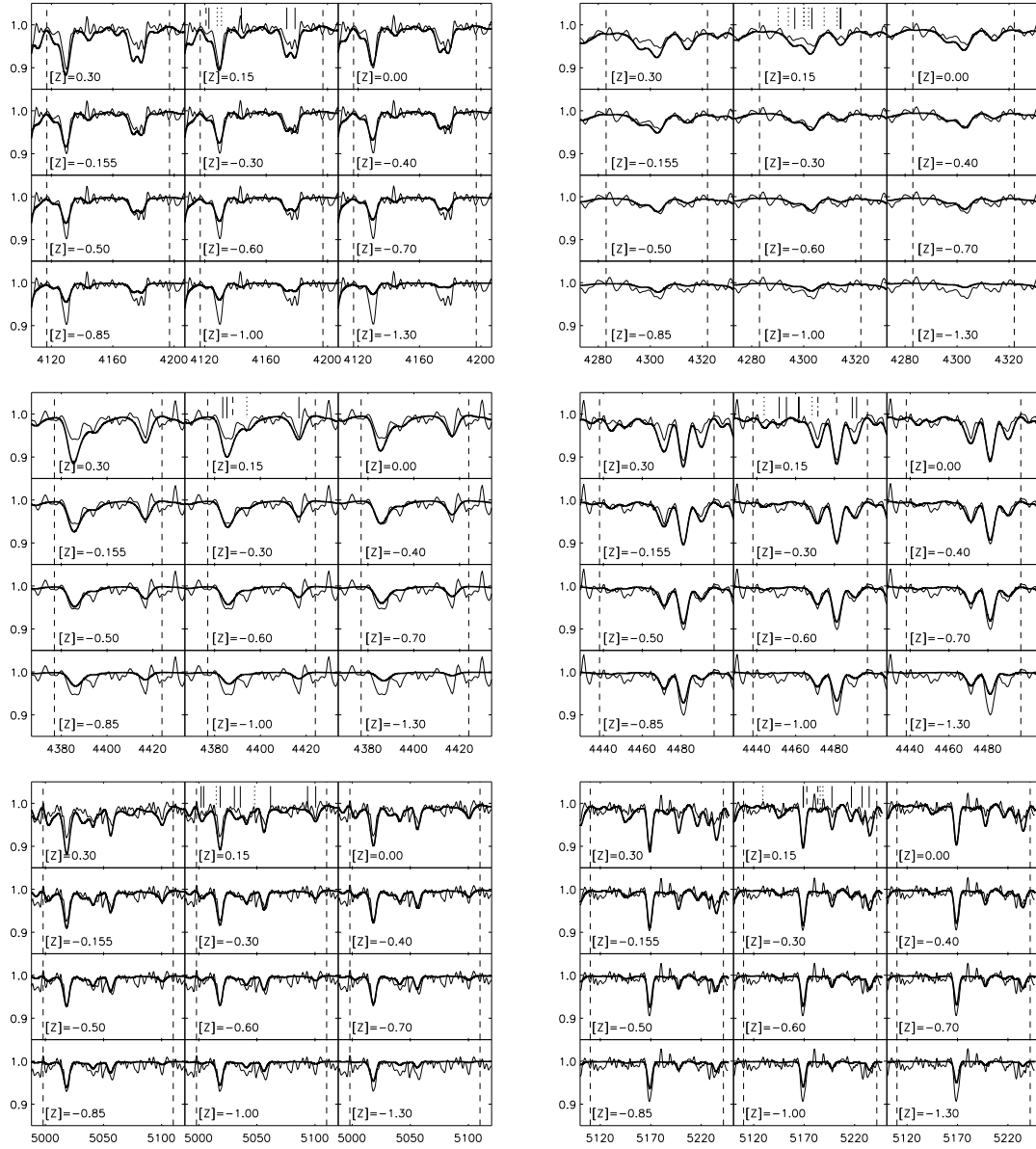


Fig. 14.— Determination of metallicity for target No. 21 in six more spectral windows. Line identifications are again given for the plots with $[Z] = 0.15$. Solid bars refer to FeII, dotted bars represent TiII in windows 2, 3, 4, 6, SiII in window 1 and HeI in window 5. Dashed bars indicate HeI in window 1 and 3 and MgII in window 4 and 6. The dashed-dotted bar in window 4 is HeI. The abscissae are wavelengths in Å.

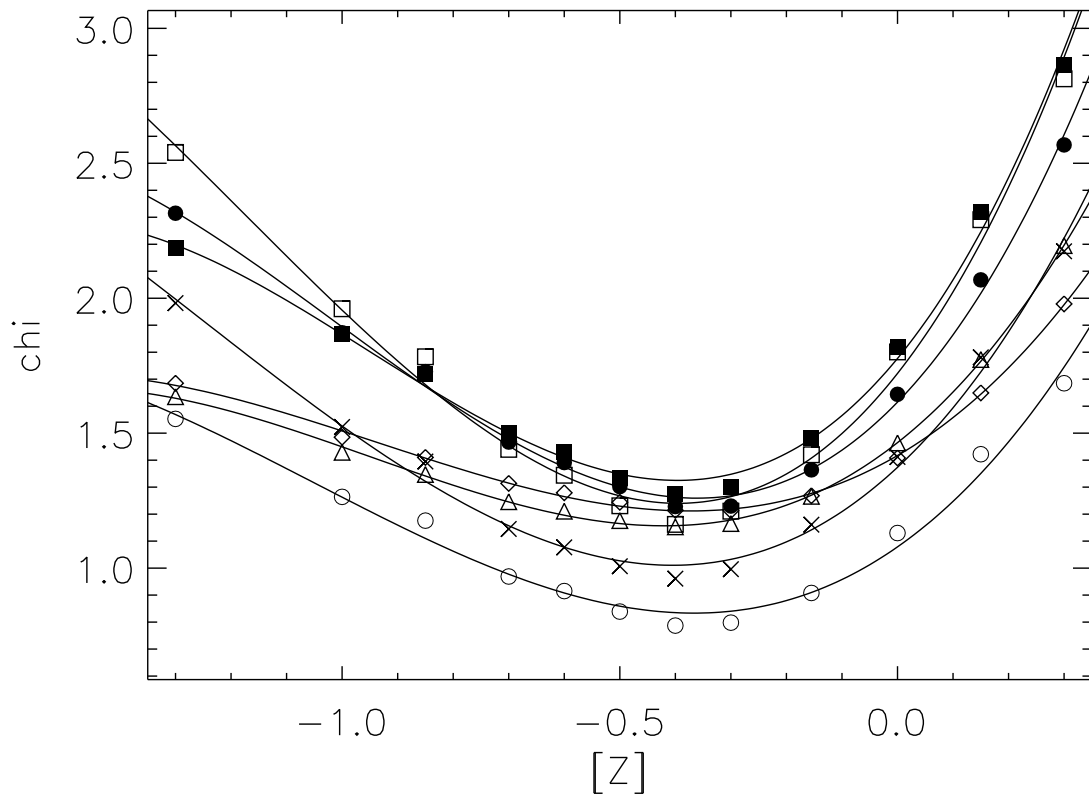


Fig. 15.— $\chi([Z])_i$ for all seven spectral windows of target No.21.

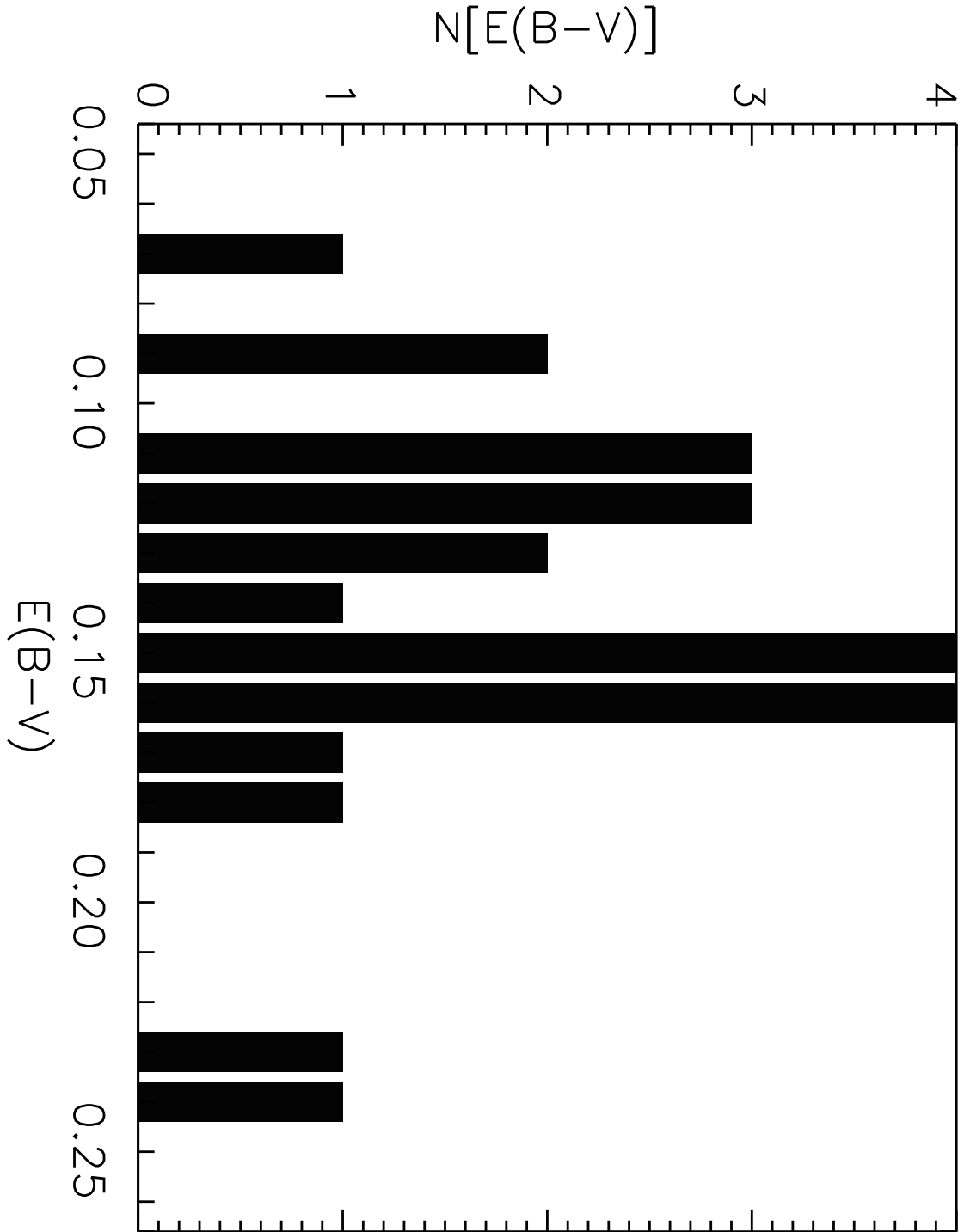


Fig. 16.— The interstellar reddening $E(B-V)$ distribution of our targets.

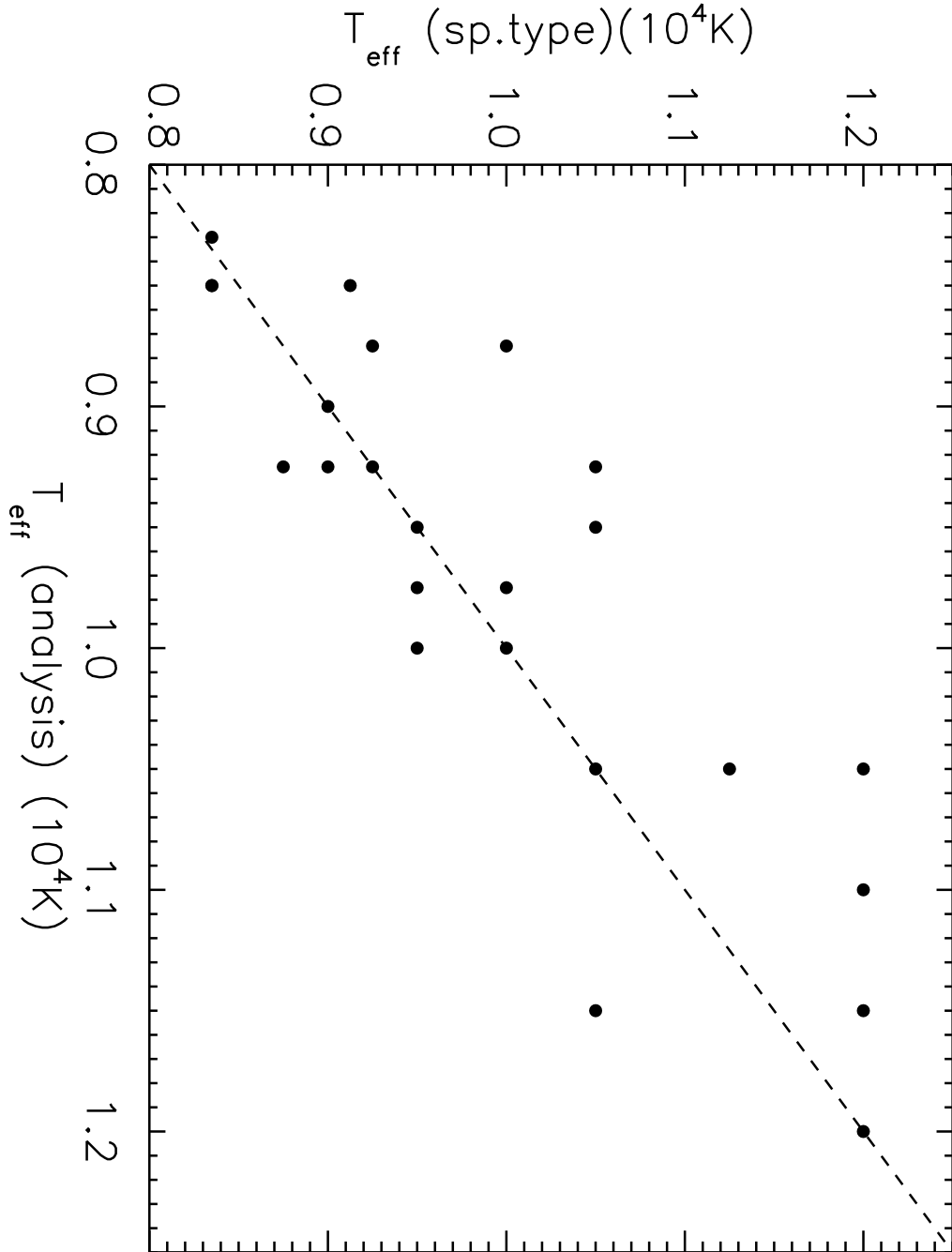


Fig. 17.— Effective temperatures according to spectral types compared with effective temperatures obtained from the quantitative spectral analysis. For discussion see text.

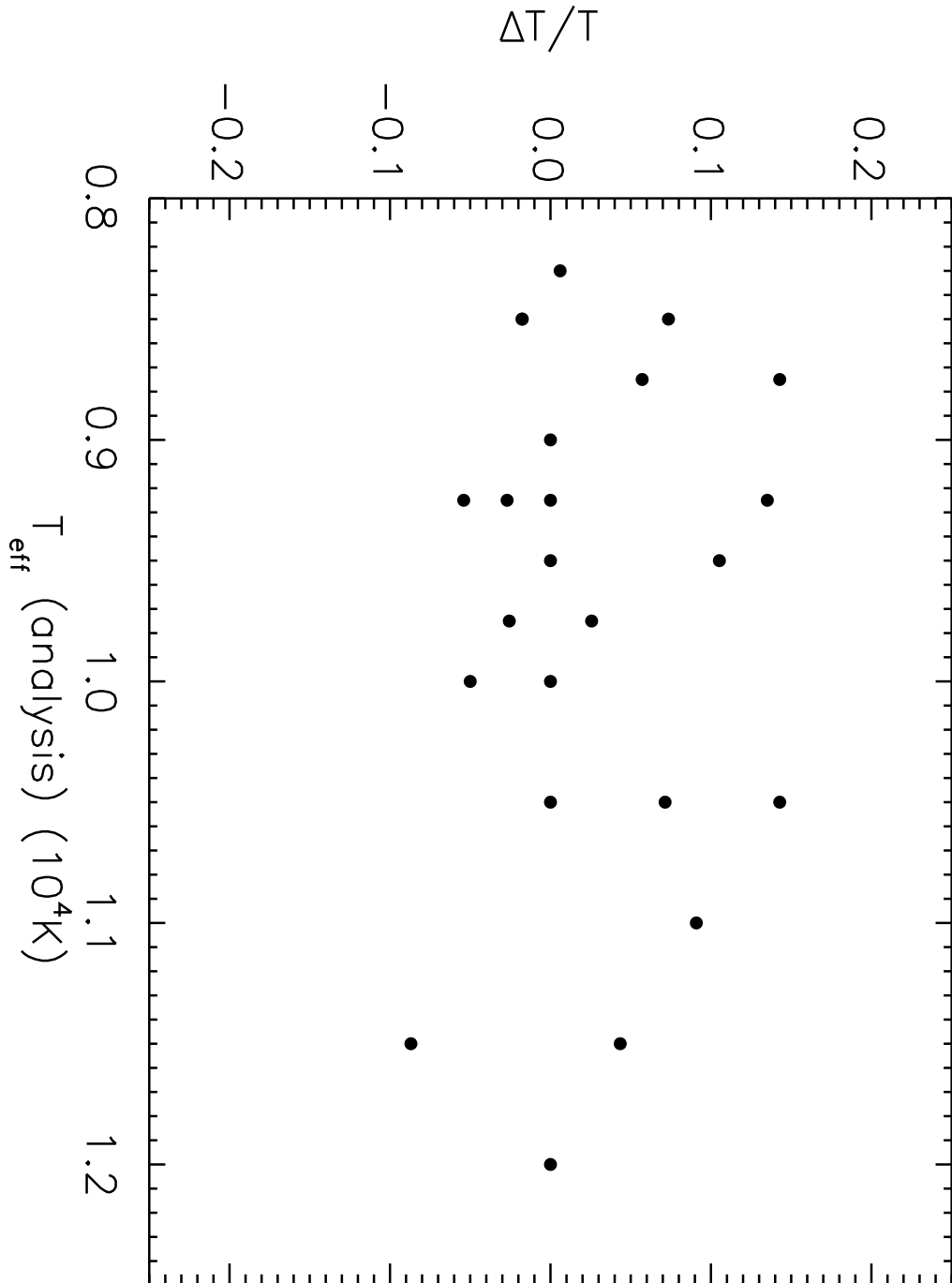


Fig. 18.— Relative difference of spectral type and spectral analysis temperatures as a function of effective temperatures obtained from the quantitative spectral analysis.

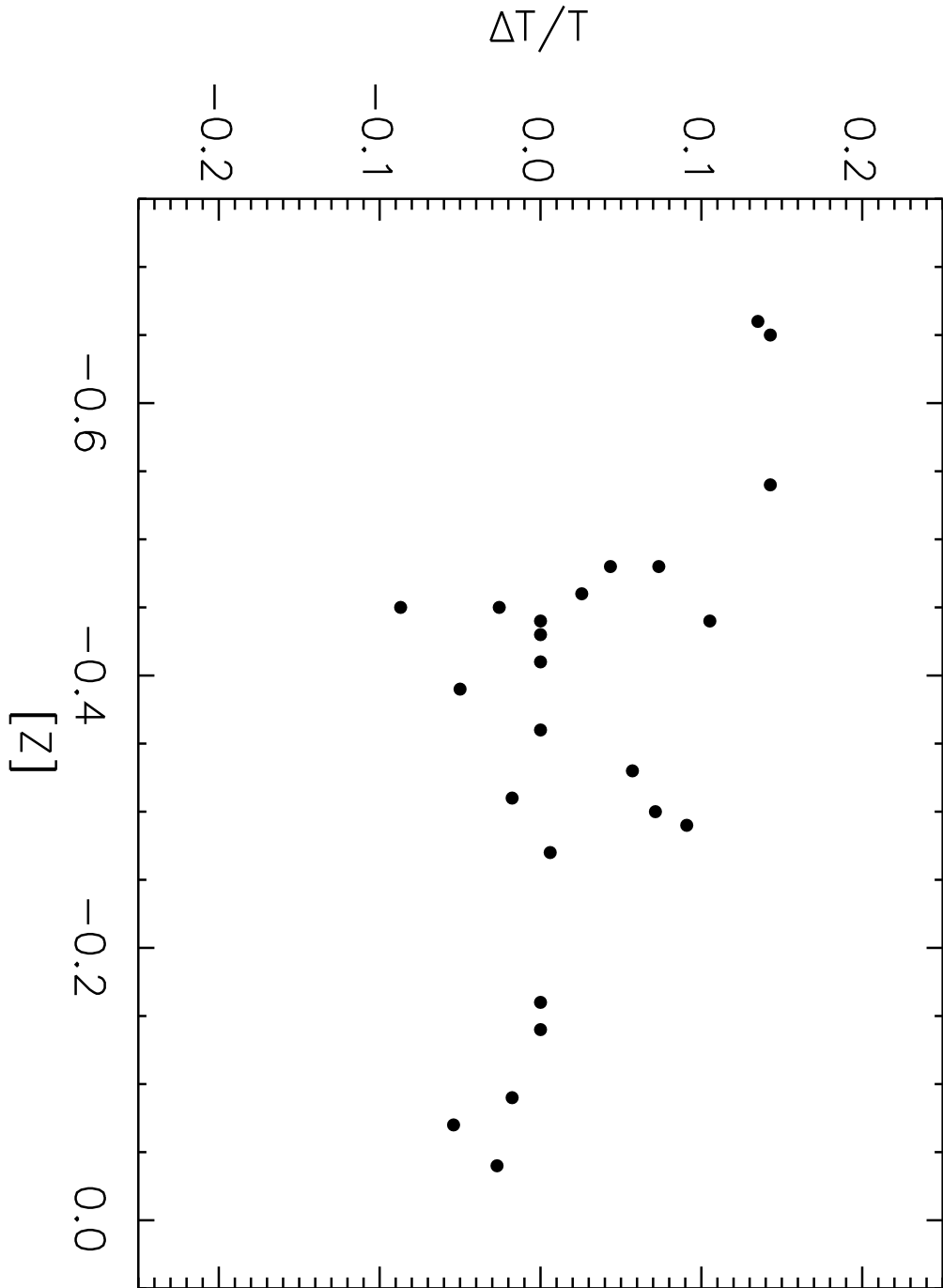


Fig. 19.— Relative difference of spectral type and analysis temperatures as a function of metallicity obtained from the quantitative spectral analysis.

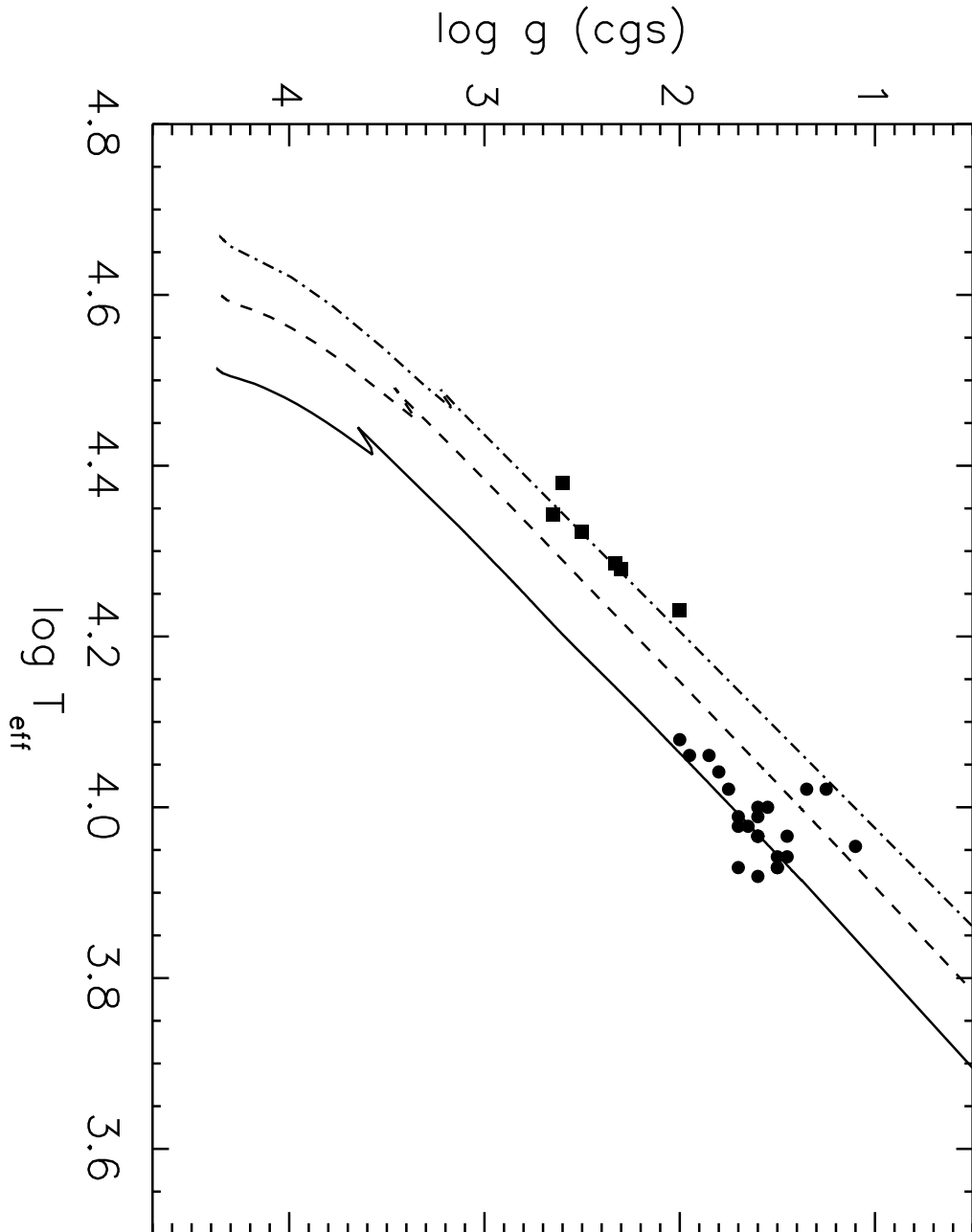


Fig. 20.— NGC 300 A supergiants (circles, this study) and early B supergiants (squares, Urbaneja et al. 2005) in the $(\log g, \log T_{\text{eff}})$ plane compared with evolutionary tracks by Meynet & Maeder (2005) of stars with 15 M_{\odot} (solid), 25 M_{\odot} (dashed), and 40 M_{\odot} (dashed-dotted), respectively. The tracks include the effects of rotation and are calculated for SMC metallicity (see Meynet & Maeder 2005).

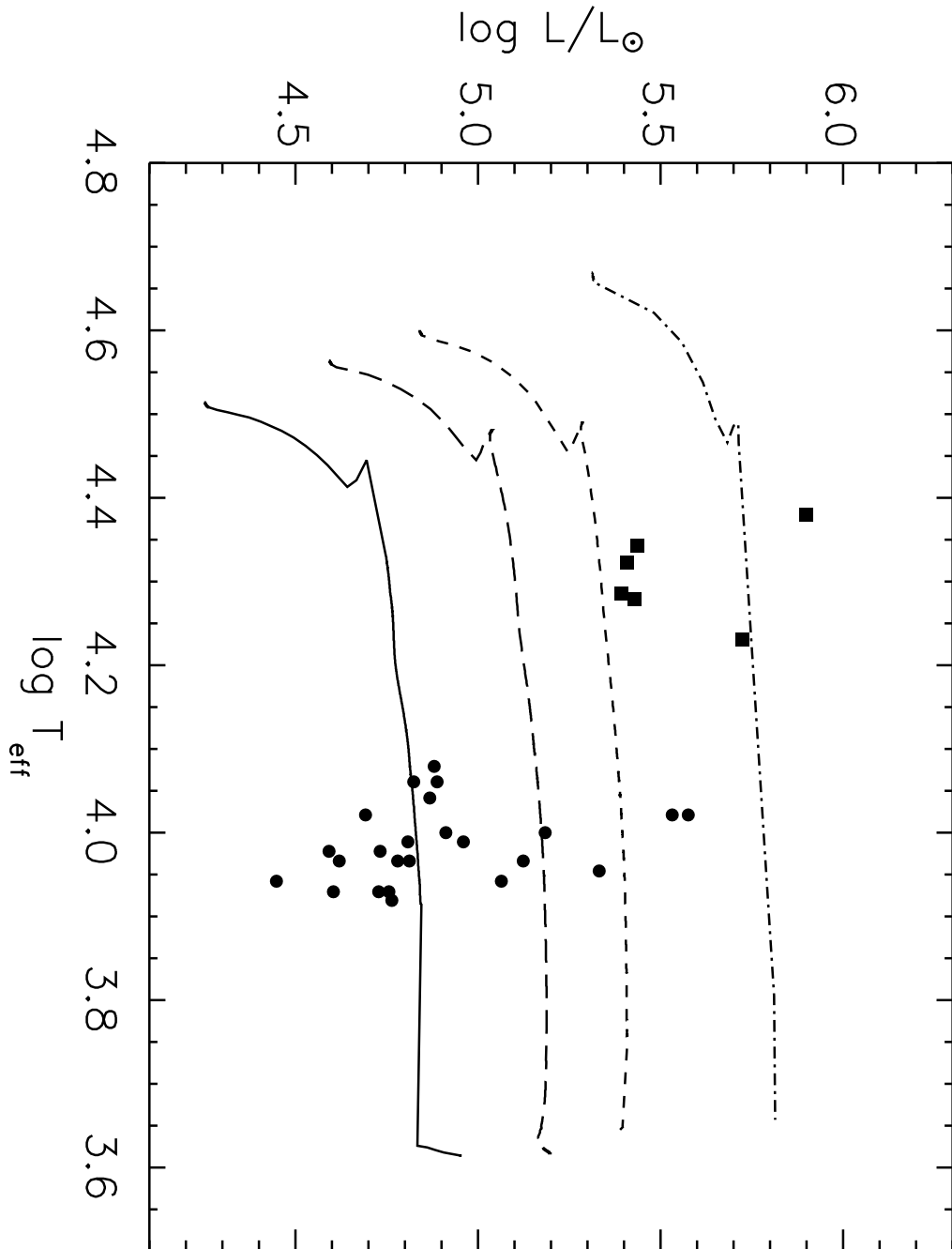


Fig. 21.— NGC 300 A supergiants (circles, this study) and early B supergiants (squares, Urbaneja et al. 2005) in the HRD compared with evolutionary tracks for stars with $15 M_{\odot}$ (solid), $20 M_{\odot}$ (long-dashed), $25 M_{\odot}$ (short-dashed), and $40 M_{\odot}$ (dashed-dotted), respectively. The tracks include the effects of rotation and are calculated for SMC metallicity (see Meynet & Maeder 2005).

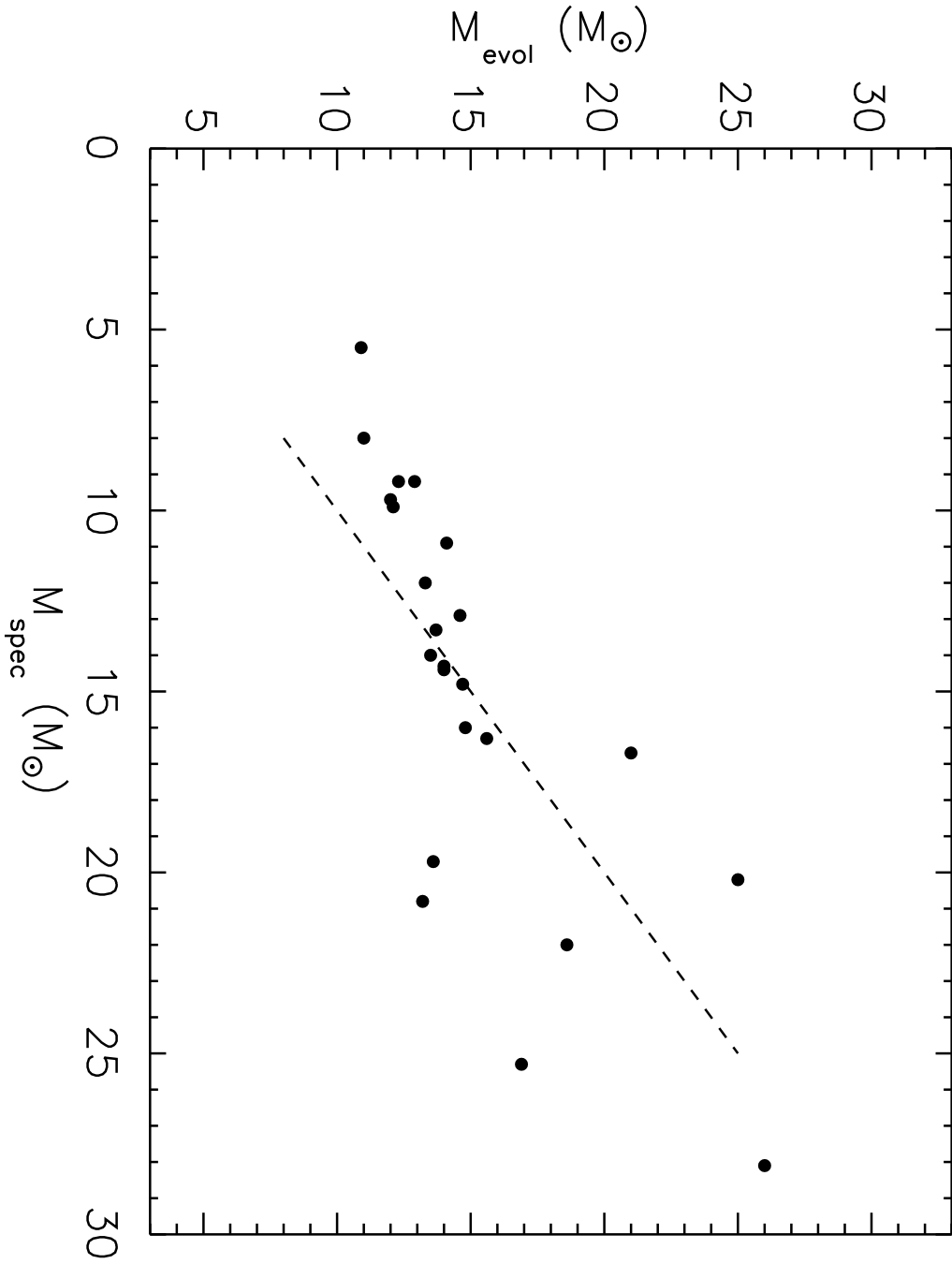


Fig. 22.— Comparison of evolutionary with spectroscopic masses for the NGC 300 A supergiants of this study

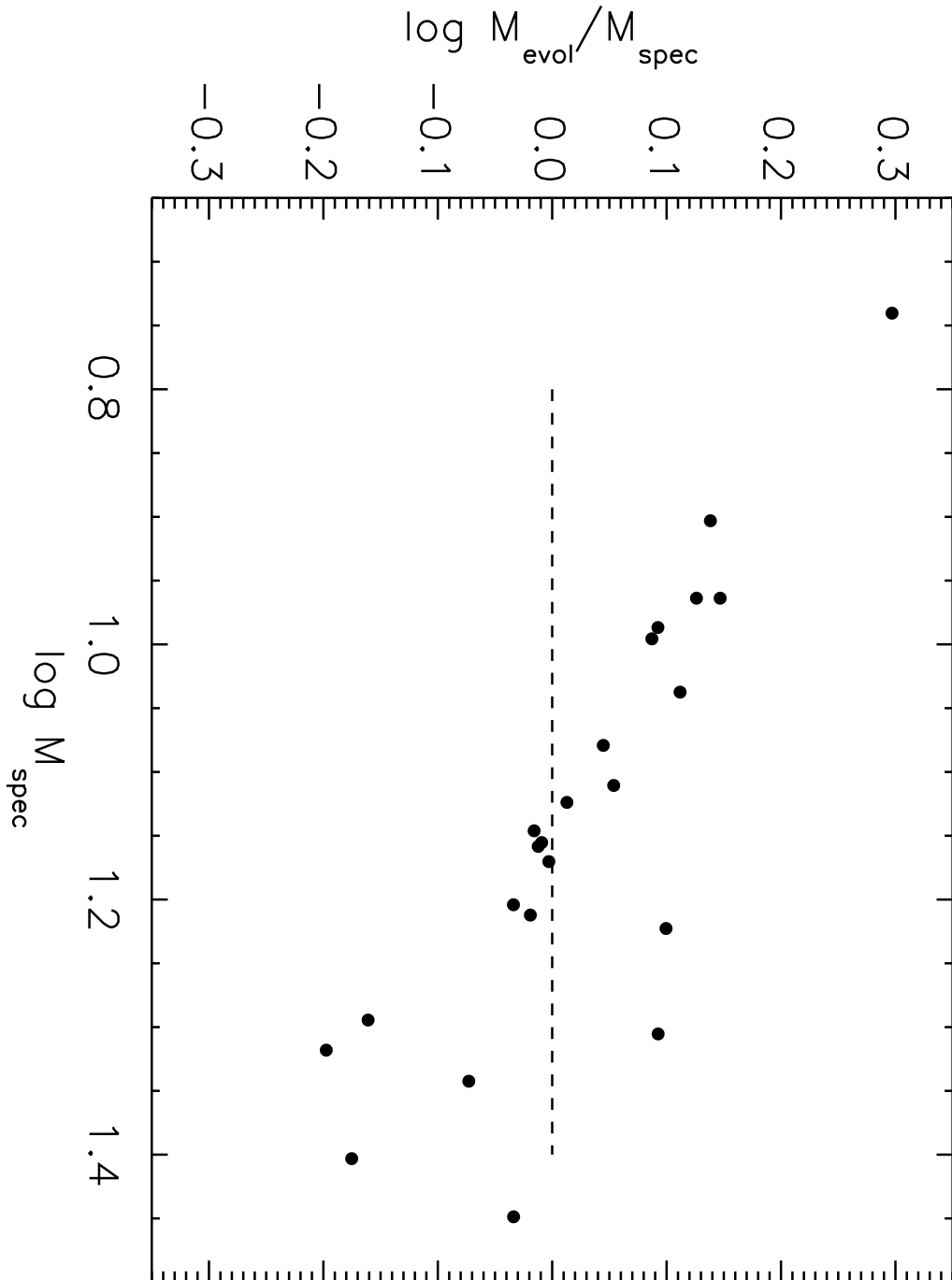


Fig. 23.— Logarithm of the ratio of evolutionary to spectroscopic masses as a function of the logarithm of spectroscopic mass.

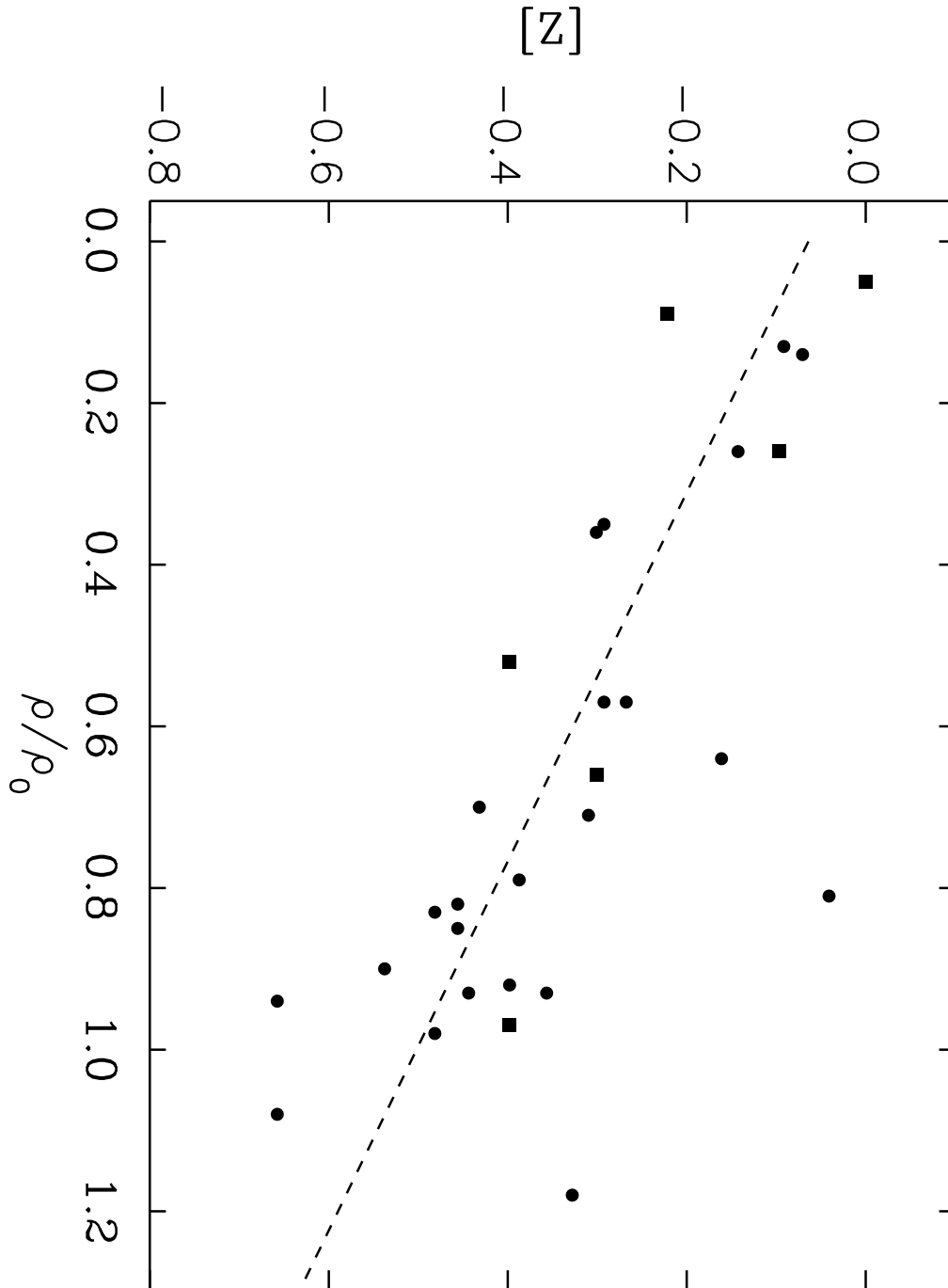


Fig. 24.— Metallicity $[Z]$ as a function of angular galacto-centric distance ρ/ρ_0 (see Table 1) for the A-supergiants of this work (filled circles) and the early B-supergiants studied by Urbaneja et al. (2005) (filled squares). Note that for the latter metallicity refers to oxygen only. The dashed curve represents the regression discussed in the text. Note that typical uncertainties in $[Z]$ are ± 0.2 dex.

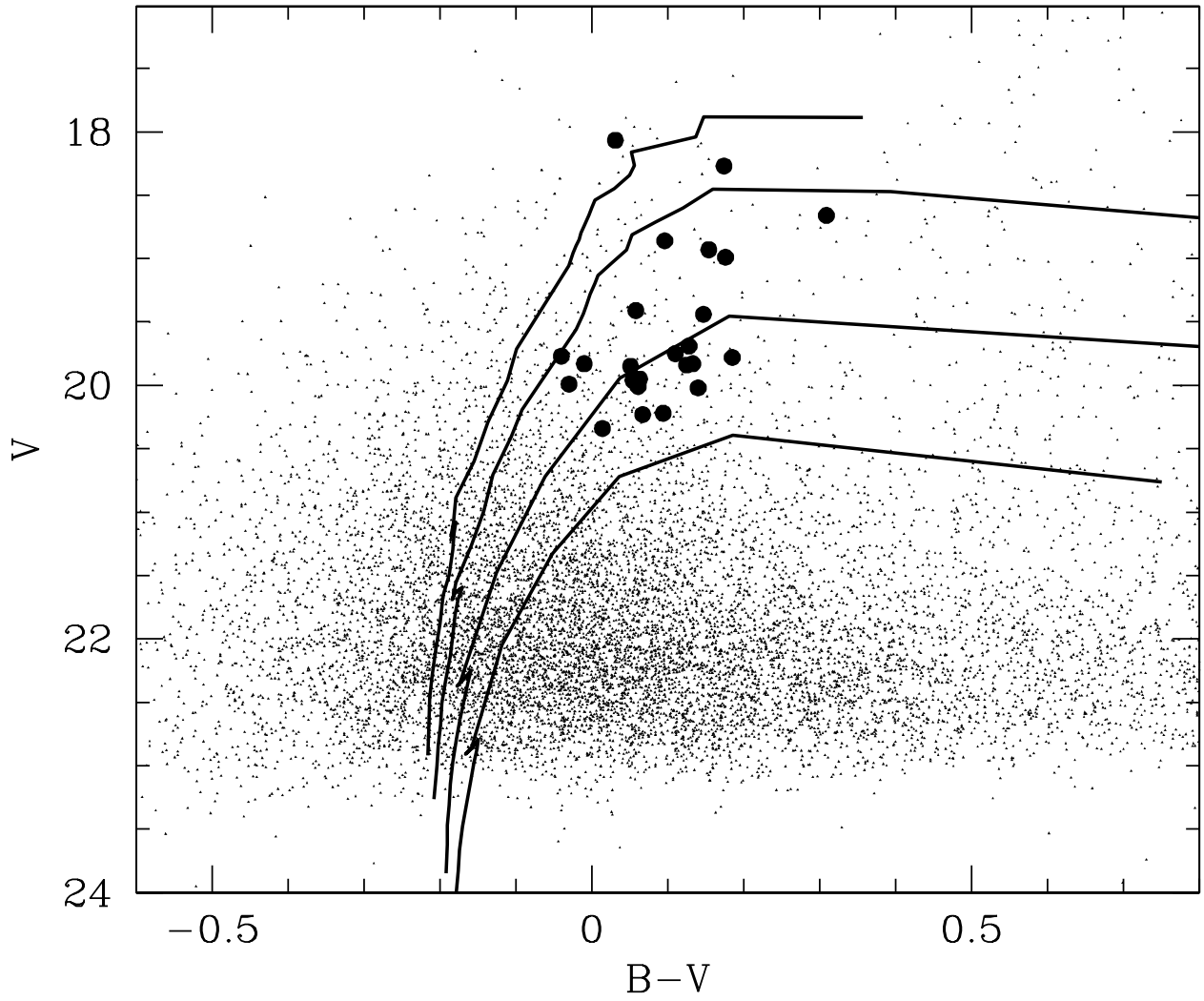


Fig. 25.— HST/ACS color magnitude diagram of the observed fields in NGC 300. The position of our targets is indicated by filled circles and evolutionary tracks (Meynet & Maeder 2005) with 12, 15, 20 and 25 M_{\odot} are overplotted.

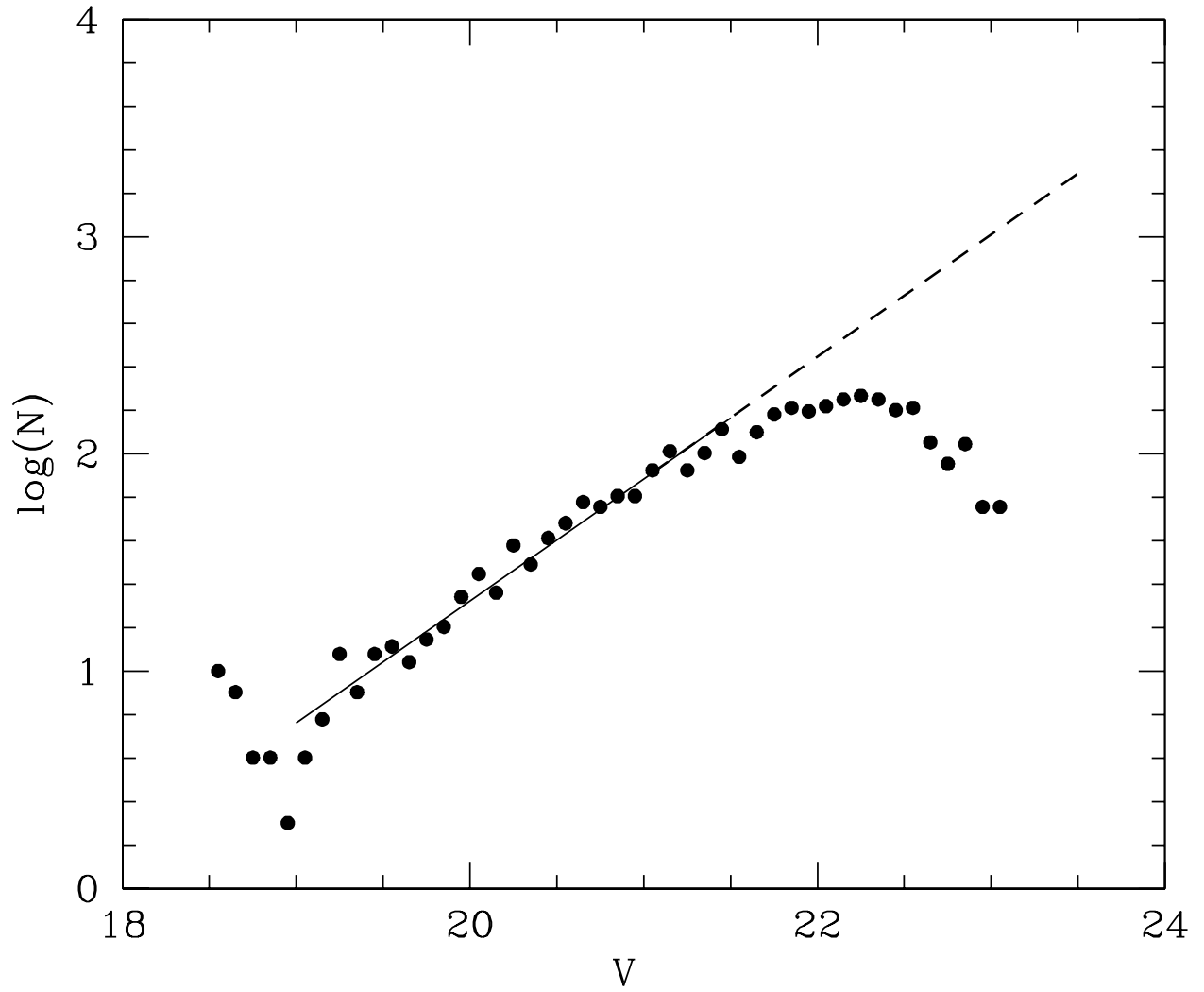


Fig. 26.— The number of stars in Fig. 25 in 0.1 magnitude bins as a function of magnitude. The fit discussed in the text is shown as a straight line.

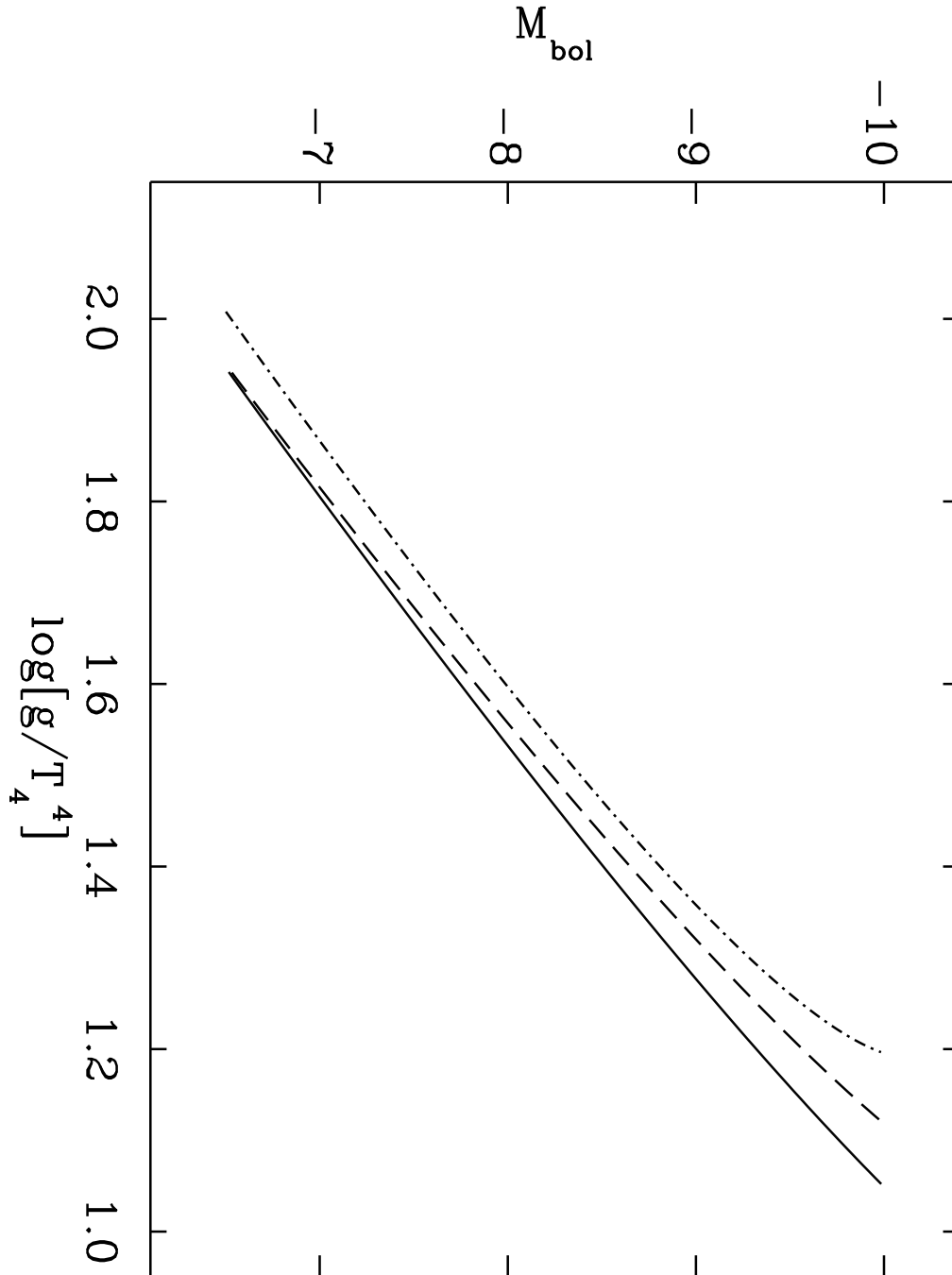


Fig. 27.— The FGLR as predicted by stellar evolution theory (Meynet & Maeder 2005) using the mass-luminosity relationship of eq. 8 and the coefficients of Table 4. The solid curve is calculated for solar metallicity and includes the effects of stellar rotation. The dashed-dotted curve is for the same metallicity but does not include rotation. The long-dashed curves assumes SMC metallicity and accounts for rotation (for this metallicity the curve without rotation is very similar).

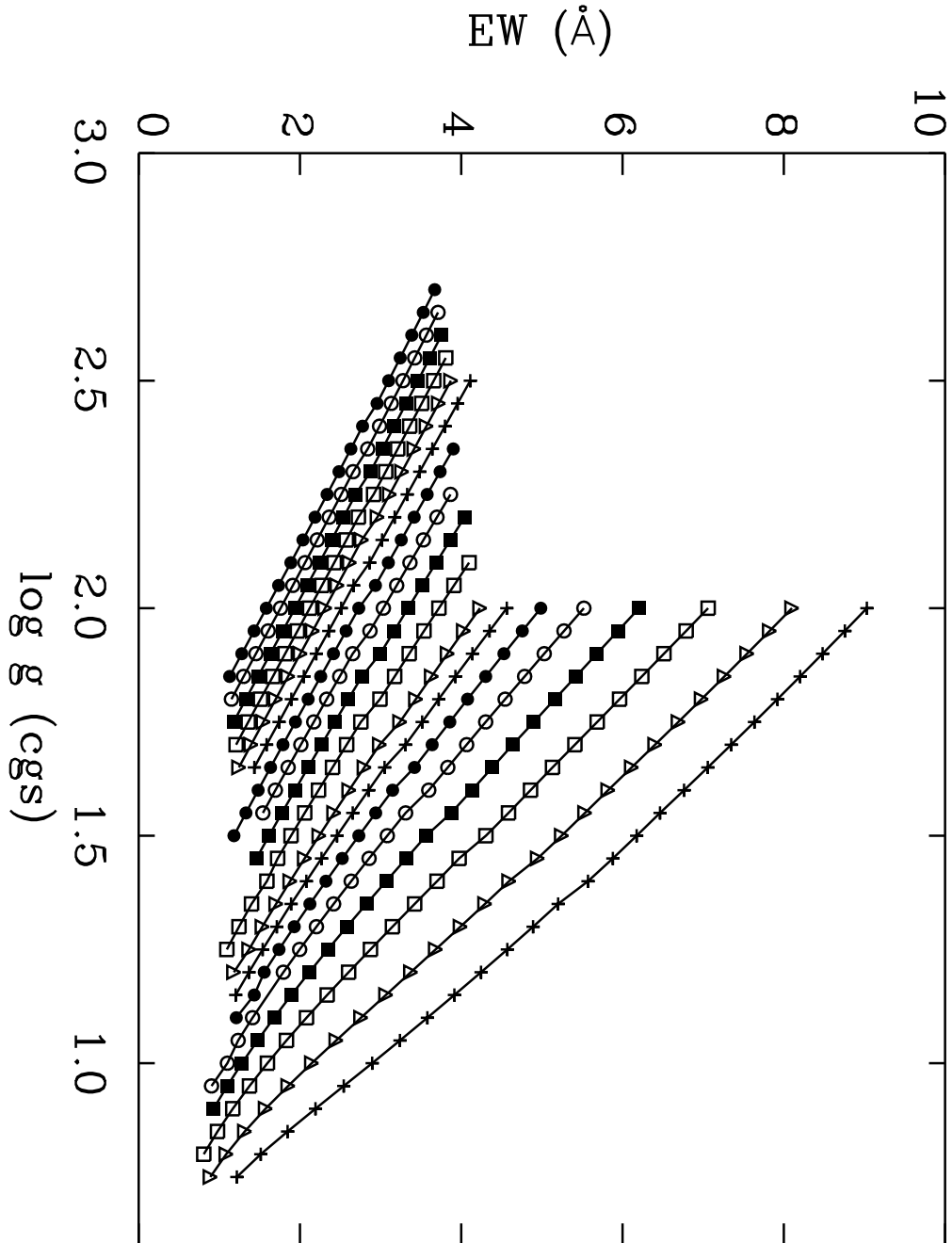


Fig. 28.— Equivalent width of H δ as a function of gravity $\log g$ for models of different effective temperature ranging between 8300 K (top curve, crosses) to 15000 K (bottom curve, filled circles). The T_{eff} steps can be inferred from Fig. 1. The metallicity is $[Z] = -0.5$, but the curves at different metallicity are very similar.

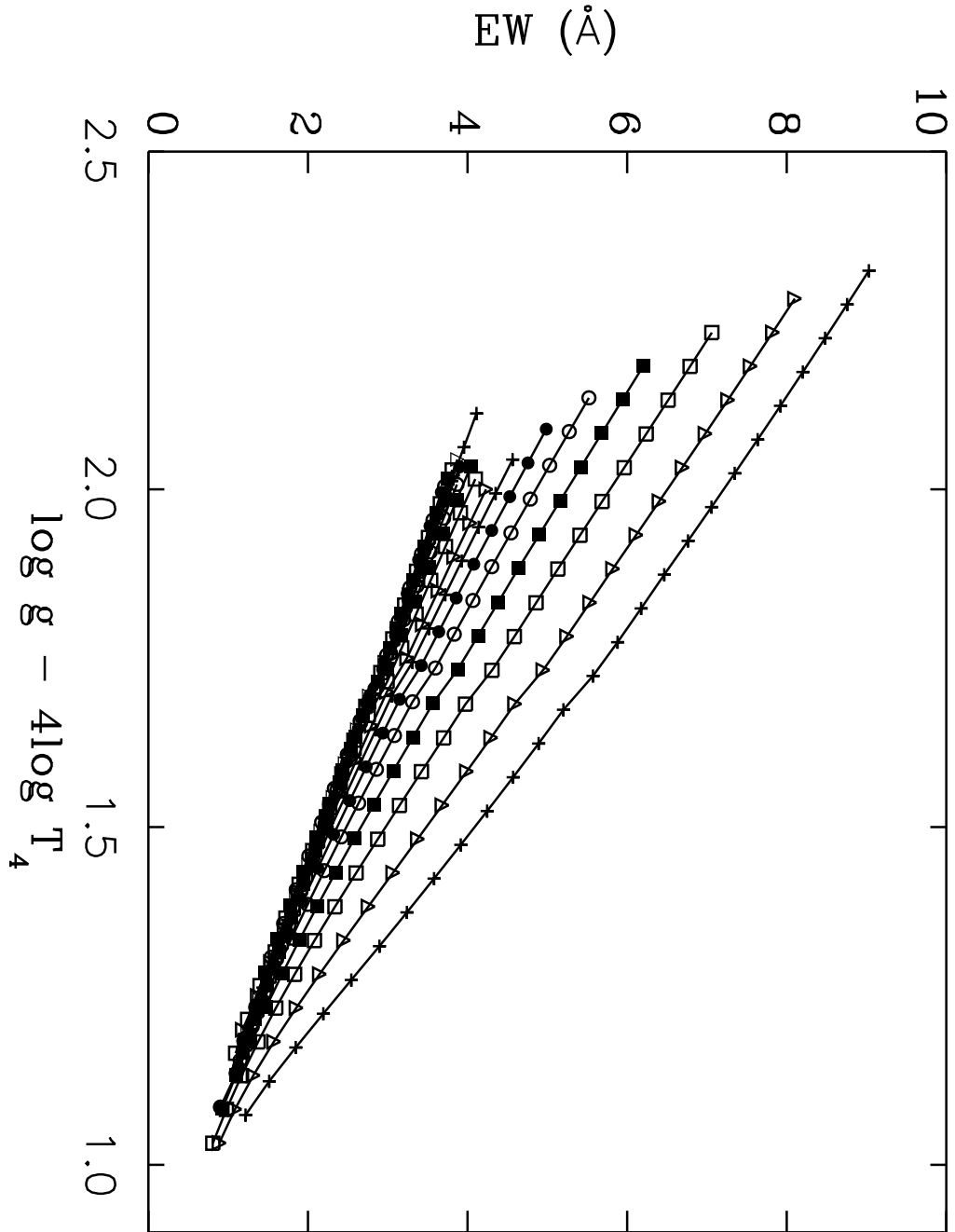


Fig. 29.— Same as Fig. 28, but for the flux weighted gravity $\log g_F$.

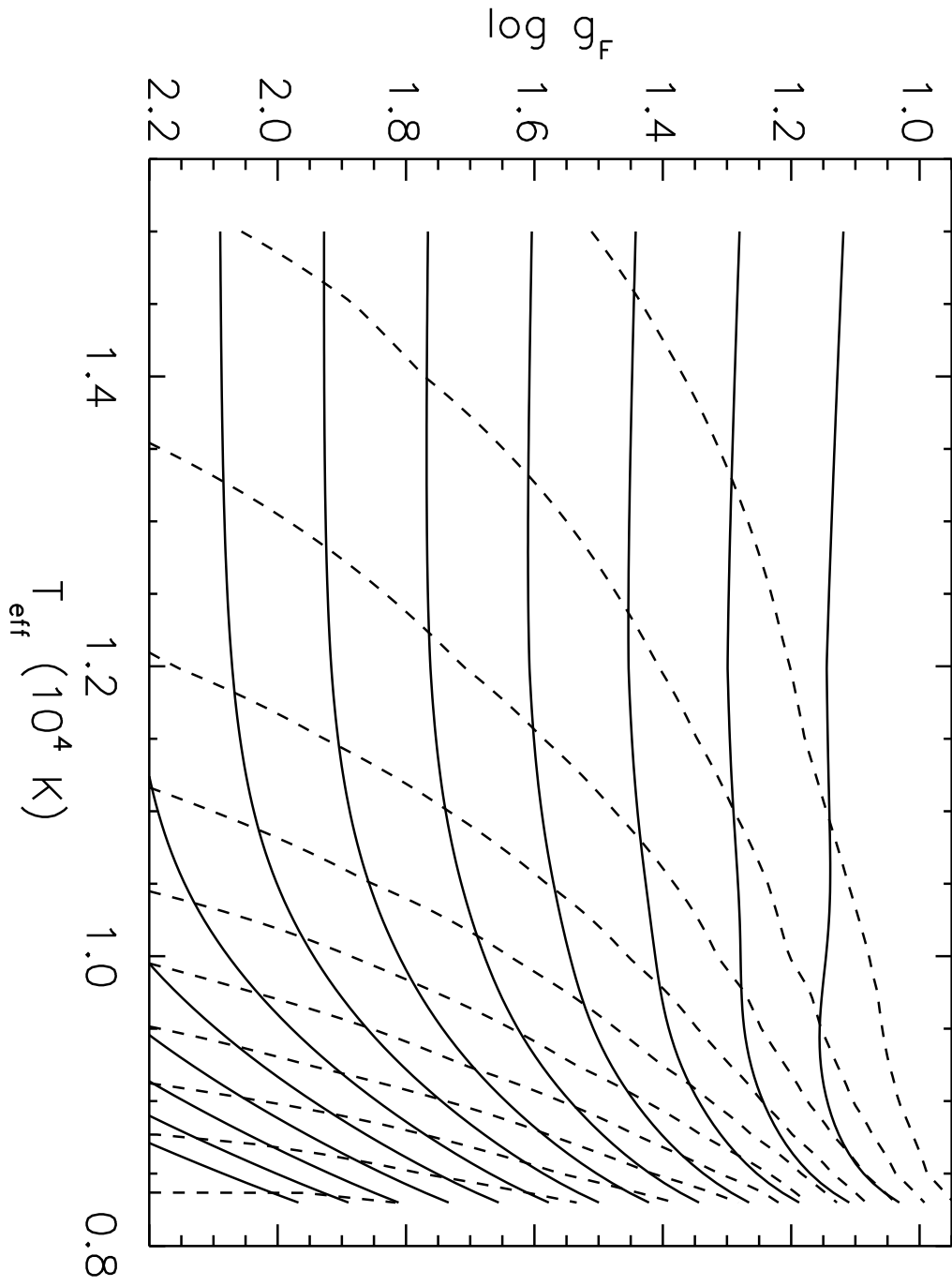


Fig. 30.— Same as Fig. 5 but for the flux weighted gravity $\log g_F$ instead of gravity $\log g$.

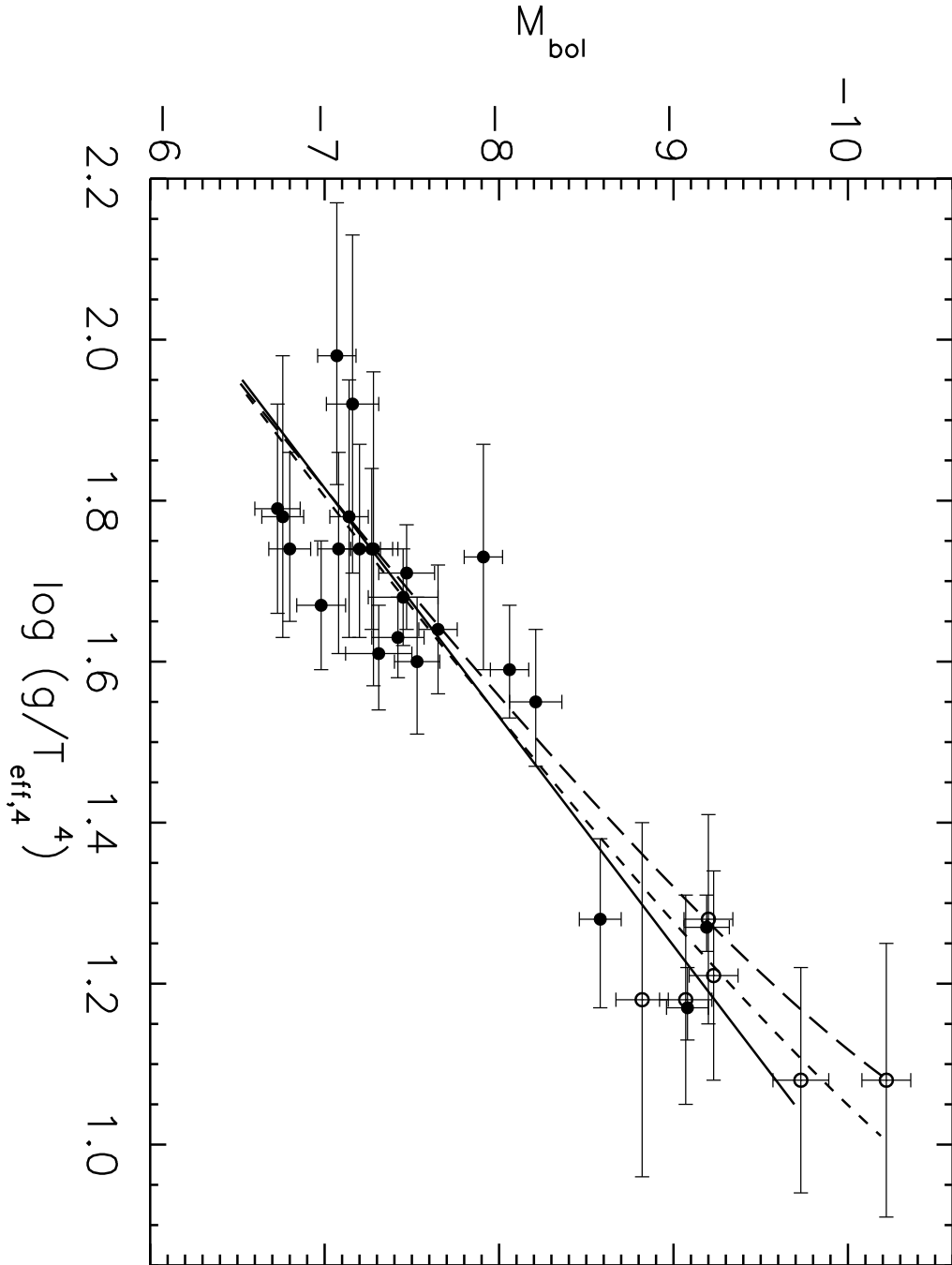


Fig. 31.— The FGLR of A (solid circles) and B (open circles) supergiants in NGC 300 and the linear regression (solid). The stellar evolution FGLRs of Fig. 27 for models with rotation are also overplotted (dashed: Milky Way metallicity, long-dashed: SMC metallicity).

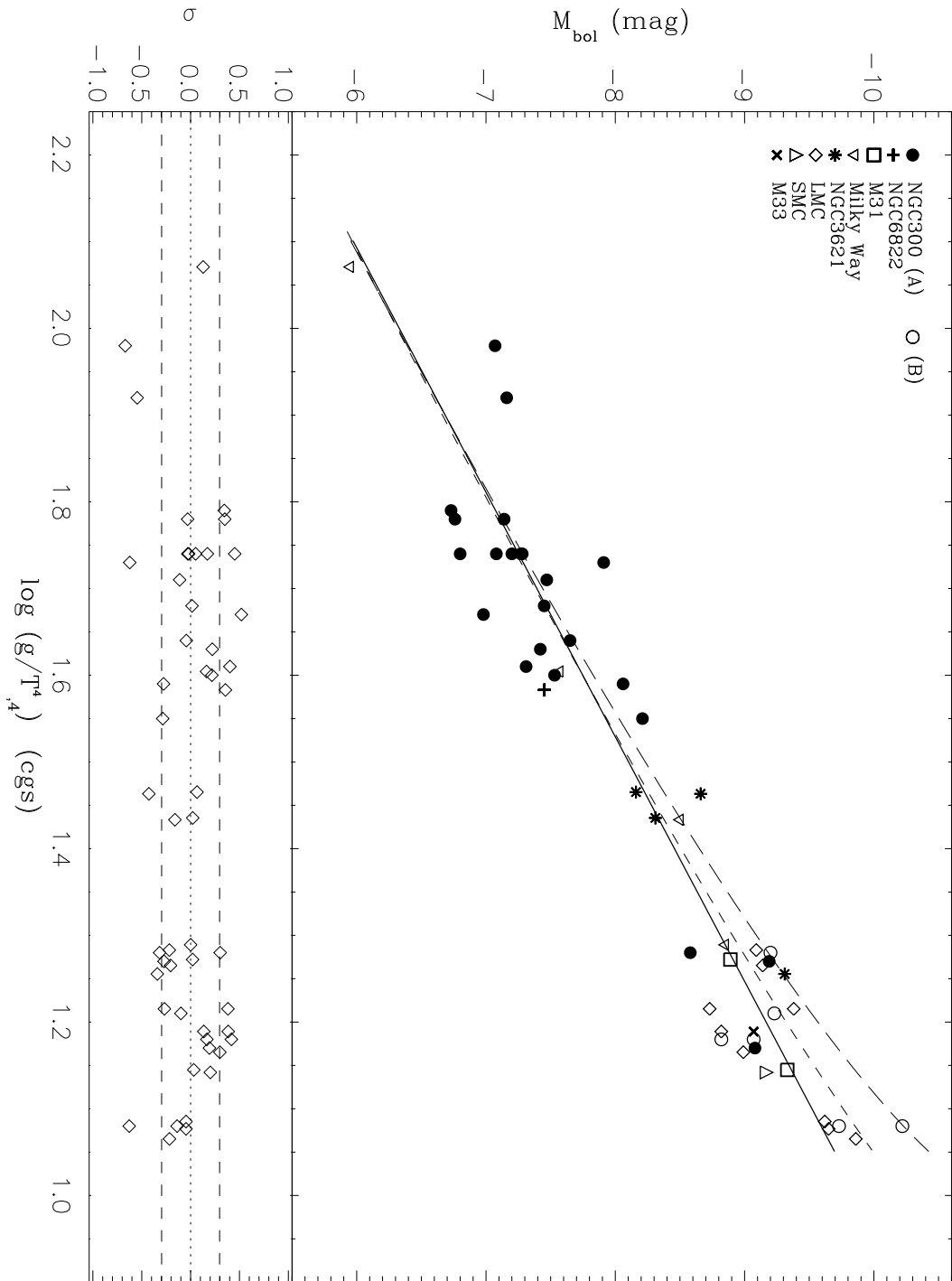


Fig. 32.— Same as Fig. 31, but with additional objects from 7 other galaxies (see text).

Table 1. NGC 300 - Spectroscopic targets and stellar parameters

No.	name	ρ/ρ_0 a	spec. type	D_B	T_{eff} K	$\log g$ cgs	$\log g_F$ cgs	[Z]	E(B-V) mag	(11)
(1)	(2)	(3)	(4)	(5)	(6)	(7)	(8)	(9)	(10)	(11)
0	A8	1.03	B9-A0		10000 ⁺⁵⁰⁰ ₋₅₀₀	1.60 ^{+0.17} _{-0.18}	1.60 ^{+0.08} _{-0.09}	-0.44±0.15	0.09	b
1	A10	0.81	A2	0.37	9250 ⁺²⁷⁰ ₋₁₃₀	1.45 ^{+0.13} _{-0.08}	1.59 ^{+0.08} _{-0.06}	-0.04±0.20	0.16	
2	A11	0.94	B8	0.08	10500 ⁺⁵⁰⁰ ₋₅₀₀	1.25 ^{+0.14} _{-0.12}	1.17 ^{+0.05} _{-0.04}	-0.65±0.15	0.16	d
3	C6	0.85	A0	0.34	9750 ⁺⁴⁰⁰ ₋₄₀₀	1.70 ^{+0.17} _{-0.18}	1.74 ^{+0.10} _{-0.10}	-0.45±0.20	0.16	
4	C16	0.70	B9	0.13	10500 ⁺⁵⁰⁰ ₋₅₀₀	1.35 ^{+0.12} _{-0.11}	1.27 ^{+0.04} _{-0.03}	-0.43±0.15	0.14	c,d
5	D12	0.64	A2	0.28	9000 ⁺⁴⁰⁰ ₋₄₀₀	1.10 ^{+0.17} _{-0.19}	1.28 ^{+0.10} _{-0.11}	-0.16±0.15	0.24	
6	A6	0.98	A1-A2	0.56	8500 ⁺²⁷⁰ ₋₂₀₀	1.50 ^{+0.22} _{-0.19}	1.78 ^{+0.17} _{-0.15}	-0.48±0.30	0.17	
7	A13	0.83	B8	0.22	11500 ⁺⁷³⁰ ₋₆₀₀	1.95 ^{+0.17} _{-0.16}	1.71 ^{+0.06} _{-0.07}	-0.48±0.30	0.11	
8	A18	0.93	B8	0.19	12000 ⁺⁹³⁰ ₋₆₇₀	2.00 ^{+0.19} _{-0.16}	1.68 ^{+0.06} _{-0.06}	-0.36±0.30	0.13	c
9	B5	0.35	B8	0.23	11000 ⁺⁶⁰⁰ ₋₅₃₀	1.80 ^{+0.14} _{-0.14}	1.63 ^{+0.05} _{-0.05}	-0.29±0.20	0.11	c
10	B8	0.26	A0		9500 ⁺⁴⁰⁰ ₋₄₀₀	1.65 ^{+0.19} _{-0.20}	1.74 ^{+0.12} _{-0.13}	-0.14±0.25	0.12	b,c
11	B10	0.14	A2-A3	0.40	9250 ⁺⁵³⁰ ₋₃₃₀	1.60 ^{+0.32} _{-0.24}	1.78 ^{+0.20} _{-0.15}	-0.07±0.30	0.15	
12	B11	0.13	A4	0.54	8500 ⁺³³⁰ ₋₂₀₀	1.50 ^{+0.27} _{-0.19}	1.74 ^{+0.22} _{-0.17}	-0.09±0.30	0.11	
13	B19	0.36	B8-B9	0.26	10500 ⁺⁵³⁰ ₋₅₃₀	1.75 ^{+0.16} _{-0.18}	1.67 ^{+0.08} _{-0.08}	-0.30±0.20	0.15	
14	C1	1.18	A1	0.49	8750 ⁺²⁷⁰ ₋₂₇₀	1.50 ^{+0.19} _{-0.20}	1.73 ^{+0.14} _{-0.14}	-0.33±0.25	0.15	
15	C8	0.92	B9	0.19	11500 ⁺⁸⁷⁰ ₋₆₇₀	1.85 ^{+0.19} _{-0.17}	1.61 ^{+0.06} _{-0.07}	-0.45±0.30	0.12	
16	C9	0.93	B9	0.39	9500 ⁺⁴⁷⁰ ₋₄₀₀	1.70 ^{+0.21} _{-0.20}	1.79 ^{+0.13} _{-0.13}	-0.44±0.30	0.12	
17	C12	0.90	B9-A0	0.49	8750 ⁺²⁷⁰ ₋₃₃₀	1.45 ^{+0.18} _{-0.23}	1.68 ^{+0.13} _{-0.16}	-0.54±0.25	0.09	
18	D2	0.57	A1	0.41	9250 ⁺⁴⁰⁰ ₋₂₇₀	1.60 ^{+0.21} _{-0.16}	1.74 ^{+0.13} _{-0.11}	-0.41±0.20	0.16	
19	D7	0.71	A4	0.56	8500 ⁺²⁷⁰ ₋₂₀₀	1.70 ^{+0.24} _{-0.20}	1.98 ^{+0.19} _{-0.16}	-0.31±0.20	0.23	c
20	D10	0.57	A4	0.63	8300 ⁺²⁷⁰ ₋₂₇₀	1.60 ^{+0.26} _{-0.26}	1.92 ^{+0.21} _{-0.21}	-0.27±0.15	0.18	c
21	D13	0.79	A0	0.27	10000 ⁺⁶⁰⁰ ₋₄₇₀	1.55 ^{+0.19} _{-0.17}	1.55 ^{+0.09} _{-0.08}	-0.39±0.15	0.13	
22	D17	0.82	B9-A0	0.32	9750 ⁺²⁷⁰ ₋₃₃₀	1.60 ^{+0.12} _{-0.15}	1.64 ^{+0.08} _{-0.08}	-0.46±0.15	0.15	
23	D18	1.08	B9	0.41	9250 ⁺³³⁰ ₋₂₀₀	1.60 ^{+0.18} _{-0.13}	1.74 ^{+0.12} _{-0.09}	-0.66±0.20	0.07	

^aGalactocentric distance, in units of the isophotal radius $\rho_0 = 9.75$ arcmin $\simeq 5.33$ kpc

^bno Balmer jump measured; T_{eff} from HeI lines

^cno HST photometry available; ground-based photometry used, see text

^dHeI lines also used for used T_{eff} , see text

Table 2. Bolometric corrections and magnitudes, radii and masses

No.	name	m_V mag	M_V ^a mag	BC mag	M_{bol} ^a mag	R/R_\odot	M/M_\odot spec	M/M_\odot evol
(1)	(2)	(3)	(4)	(5)	(6)	(7)	(8)	(9)
0	A8	19.41	-7.24	-0.29	-7.53±0.13	96	13.2	15.7
1	A10	18.93	-7.94	-0.12	-8.06±0.05	142	20.8	18.8
2	A11	18.27	-8.59	-0.49	-9.08±0.12	177	20.2	27.7
3	C6	19.84	-7.01	-0.26	-7.27±0.12	89	14.4	14.4
4	C16	18.07	-8.75	-0.44	-9.19±0.13	186	28.1	29.0
5	D12	18.66	-8.45	-0.13	-8.58±0.04	191	16.7	22.7
6	A6	19.78	-7.11	-0.03	-7.14±0.05	110	14.0	13.9
7	A13	19.85	-6.86	-0.61	-7.47±0.13	70	16.0	15.4
8	A18	19.99	-6.79	-0.66	-7.45±0.17	64	14.8	15.3
9	B5	19.77	-6.94	-0.48	-7.42±0.11	75	12.9	15.2
10	B8	19.83	-6.89	-0.19	-7.08±0.12	86	12.0	13.6
11	B10	19.69	-7.14	-0.14	-7.28±0.10	99	14.3	14.5
12	B11	19.95	-6.76	0.00	-6.76±0.06	93	9.9	12.3
13	B19	20.23	-6.60	-0.38	-6.98±0.06	67	9.2	13.2
14	C1	18.99	-7.85	-0.06	-7.91±0.05	148	25.3	17.8
15	C8	20.01	-6.74	-0.57	-7.31±0.16	65	10.9	14.6
16	C9	20.22	-6.52	-0.21	-6.73±0.09	73	9.7	12.2
17	C12	20.34	-6.31	-0.06	-6.37±0.04	73	5.5	11.0
18	D2	19.83	-7.04	-0.16	-7.20±0.07	96	13.3	14.1
19	D7	20.02	-7.06	-0.01	-7.07±0.05	107	20.8	13.6
20	D10	19.75	-7.18	0.02	-7.16±0.05	117	19.7	13.9
21	D13	18.86	-7.92	-0.29	-8.21±0.11	131	22.0	19.8
22	D17	19.44	-7.40	-0.25	-7.65±0.05	106	16.3	16.3
23	D18	19.96	-6.62	-0.18	-6.80±0.06	80	9.2	12.5

^adistance modulus = 26.37 mag, Gieren et al. (2005a)

Table 3. Central metallicity [Z] and metallicity gradient in NGC 300

Source	Central abundance dex	Gradient ρ/ρ_0	Gradient dex/kpc	Comments
(1)	(2)	(3)	(4)	(5)
Dopita & Evans(1986)	0.26±0.17	-0.63±0.10	-0.118±0.019	HII, oxygen
Zaritsky et al. (1994)	0.29±0.04	-0.54±0.09	-0.101±0.017	HII, oxygen
Kobulnicky et al. (1999)	0.06±0.04	-0.27±0.09	-0.051±0.017	HII, oxygen
Denicolo et al. (2002)	-0.08±0.05	-0.46±0.10	-0.086±0.019	HII, oxygen
Pilyugin (2001)	-0.17±0.06	-0.28±0.12	-0.053±0.023	HII, oxygen
Pettini & Pagel (2004)	-0.19±0.04	-0.36±0.08	-0.068±0.015	HII, oxygen
This work	-0.06±0.09	-0.44±0.12	-0.083±0.023	stars, metals

Table 4. Fit coefficients for stellar evolution mass-luminosity relationship and FGLR

Model	Metallicity	a	b	c	$\log(M^{min}/M_{\odot})$	α_0	α_1	α_2	x_0	M_{bol}^0
(1)	(2)	(3)	(4)	(5)	(6)	(7)	(8)	(9)	(10)	(11)
with rotation	Milky Way	3.80	1.40	4.095	0.943	3.505	0.15	0.30	1.957	-6.464
with rotation	SMC	3.10	1.20	4.560	1.077	3.659	0.32	0.32	1.967	-6.439
no rotation	Milky Way	4.25	2.00	3.825	0.943	–	–	–	–	–
no rotation	SMC	4.10	2.05	4.030	0.954	–	–	–	–	–

Table 5. Stellar parameters of A supergiants in 7 galaxies

No.	name	galaxy	m-M mag	T_{eff} K	$\log g$ cgs	M_{bol} mag	comments
(1)	(2)	(3)	(4)	(5)	(6)	(7)	(8)
0	η Leo	Milky Way	9.00	9600	2.00	-5.73	a
1	HD111613	Milky Way	11.80	9150	1.45	-7.43	a
2	HD92207	Milky Way	12.40	9500	1.20	-9.04	a
3	Rigel	Milky Way	7.80	12000	1.75	-8.49	a
4	Deneb	Milky Way	9.50	8525	1.10	-8.48	b
5	HD12953	Milky Way	11.80	9250	1.20	-8.08	c,d
5	HD14489	Milky Way	11.80	9000	1.35	-7.81	c,d
5	HD223385	Milky Way	12.00	8500	0.95	-8.43	c,d
6	Sk-69 211	LMC	18.50	11000	1.30	-9.00	e
7	Sk-67 17	LMC	18.50	10500	1.20	-9.53	e
8	Sk-67 207	LMC	18.50	10000	1.20	-8.50	e
9	Sk-66 58	LMC	18.50	9500	1.10	-8.74	e
10	Sk-67 201	LMC	18.50	10000	1.20	-9.14	e
11	Sk-69 239	LMC	18.50	10000	1.05	-9.68	e
12	Sk-69 170	LMC	18.50	10000	1.20	-8.89	e
13	Sk-69 299	LMC	18.50	8750	1.00	-8.93	e
14	Sk-67 44	LMC	18.50	8000	0.65	-9.54	e
15	AV457	SMC	19.00	8500	0.90	-9.10	e
16	41-3654	M31	24.47	9200	1.00	-9.08	f,k
16	41-3712	M31	24.47	8850	1.00	-8.79	f,k
17	117-A	M33	24.47	9500	1.10	-8.29	g,d
18	NGC6822m	NGC 6822	23.31	9000	1.40	-7.23	h,i
19	No. 1	NGC 3621	29.08	9250	1.30	-8.21	d,j
20	No. 9	NGC 3621	29.08	9250	1.12	-9.20	d,j
21	No. 16	NGC 3621	29.08	10500	1.55	-8.05	d,j
22	No. 17	NGC 3621	29.08	8350	1.15	-8.58	d,j

^aPrzybilla et al. (2006)

^bSchiller & Przybilla (2007)

^cKudritzki et al. (1999)

^dKudritzki, Bresolin & Przybilla (2003)

^ethis work

^fPrzybilla et al. (2008)

^gdistance modulus from Bonanos et al. (2006)

^hdistance modulus from Gieren et al. (2006)

ⁱPrzybilla (2002)

^jBresolin et al. (2001)

^kdistance modulus from Holland (1998)

